



# **Dynamics of the Zambezi River Plume**

A dissertation submitted for the partial fulfilment of the requirements for the  
Degree of Master of Sciences in  
Applied Physical Oceanography

Fialho P. J. NEHAMA

United Kingdom  
September 2008

This thesis is dedicated to my parents  
and to my two little nieces, Charlize and Fernanda.

## **DECLARATION & STATEMENTS**

This work has not previously been accepted in substance for any degree and is not being concurrently submitted for any degree.

This dissertation is being submitted in partial fulfilment of the requirement of M.Sc. Applied Physical Oceanography.

This dissertation is the result of my own independent work / investigation, except where otherwise stated.

Other sources are acknowledged by footnotes giving explicit references. A bibliography is appended.

I hereby give consent for my dissertation, if accepted, to be made available for photocopying and for inter-library loan, and the title and summary to be made available to outside organisations.

**Signed** .....

**Date** .....

## ABSTRACT

Freshwater discharges from river runoff into the ocean have an important influence on the dynamics of many coastal regions. The plumes resulting from the encounter between fresh and saline waters have a variety of impacts, including changes in the availability of biological resources. Although there have been several general studies on the plume dynamics (and their relation to the rainfall), no quantitative analysis of the relationship between river plumes and its main controlling factor (i.e. the river discharge) has yet been reported.

In order to establish a relationship between the river discharge and the plume size, both two-dimensional particle-tracking two-layer model and satellite ocean-colour observations were used for the Zambezi River plumes in Mozambique. The model included a random walk component, and it was run under realistic windstress and river discharge conditions. Discrete particles of freshwater released every 30 minutes, the counting of which allowed the computation of the plume size, were used to parameterize the river discharge. On the other hand, the observed plume size was estimated using the red to blue ratio of the normalized water-leaving radiation from 73 MODIS-Aqua images that spanned 5 years. The plume size obtained by these two methods was correlated with the river discharge measured at the Tete gauge station.

Both model and imagery have revealed that the Coriolis deflection plays a predominant role in the dispersion patterns of the Zambezi plumes. The time lag between the river discharge and the maximum plume size was 17 days for near field plumes and 7 days for the far-field plumes. Ninety percent (90%) of the freshwater volume discharged per day was found to be diluted or dispersed in the same day. The area-runoff relation is dependent on the time of the year, and for the plumes observed in the far field during the period January-March (i.e. when the discharges are at their maximum), this relation is linear with a slope of  $1.74 \times 10^{-3} \text{ s m}^{-1}$ . For the same period, the model has reproduced a similar relation with a slope of  $1.73 \times 10^{-3} \text{ s m}^{-1}$ .

Fialho PJ Nehama

# CONTENTS

|  |           |
|--|-----------|
| <b>Abstract</b>  | <b>iv</b> |
| Acknowledgements   | vii       |
| List of figures and tables   | viii      |
| <b>1 Introduction</b>  | <b>1</b>  |
| 1.1. Background  | 1         |
| 1.2. Study site  | 2         |
| 1.3. Objectives  | 4         |
| 1.4. Research methodology  | 5         |
| 1.4.1. Numerical modelling   | 5         |
| 1.4.2. Satellite observation   | 5         |
| 1.5. Outline of thesis   | 6         |
| <b>2 Dynamics of a river plume</b>                                       | <b>7</b>  |
| 2.1. Plume characterization  | 7         |
| 2.1.1. Spatial distribution of properties                                | 8         |
| 2.1.2. Dimensionless parameter   | 11        |
| 2.2. Existing models   | 12        |
| 2.3. Discussion and approach   | 16        |
| <b>3 Parameterisation</b>  | <b>20</b> |
| 3.1. Introduction  | 20        |
| 3.2. Model Domain  | 20        |
| 3.3. Parameterization  | 21        |
| 3.4. Discussion  | 23        |
| <b>4 Numerical modelling</b>   | <b>25</b> |
| 4.1. Introduction  | 25        |
| 4.1.2. Model runs  | 25        |
| 4.2. Results   | 26        |
| 4.2.1. Model input   | 26        |
| 4.2.2. Plume characterization  | 29        |
| 4.2.3. The relationship between plume area and runoff, and/or windstress | 30        |
| 4.3. Discussion  | 33        |
| <b>5 Using satellite imagery to assess plume dimensions</b>              | <b>37</b> |
| 5.1. Introduction  | 37        |
| 5.2. Satellite remote sensing of salinity                                | 37        |
| 5.2.1. Some examples of satellite assessment of plume dimensions         | 40        |
| 5.3. Satellite image processing  | 42        |
| 5.4. Discussions and approach  | 43        |
| <b>6 Analysis of satellite data</b>                                      | <b>45</b> |
| 6.1. Introduction  | 45        |
| 6.2. Methods   | 45        |
| 6.3. Results   | 47        |
| 6.3.1. Plume characterization  | 47        |
| 6.3.2. Reflectance ratio as plume indicator                              | 49        |
| 6.3.3. River discharge and plume size relationship                       | 55        |

|  |           |
|--|-----------|
| 6.3.4. Effect of windstress              | 59        |
| 6.3.5. Comparison with model results     | 63        |
| 6.4. Discussion                          | 64        |
| 6.4.1. Plume assessed by satellite data  | 64        |
| 6.4.2. Comparison with model results     | 66        |
| <b>7 Conclusions and recommendations</b> | <b>68</b> |
| 7.1. General                             | 68        |
| 7.2. Conclusions                         | 69        |
| 7.3. Recommendations                     | 70        |
| <b>References</b>                        |           |
| Appendices                               |           |

## **ACKNOWLEDGEMENTS**

In the first place, my work could have never been done without the Nuffield Foundation. I am thankful to Dr. Dave Bowers, Dr. Lewis Le Vay, Dr. Fernando Loforte, and Dr. Antonio Hogueane who have joined the Nuffield Foundation Grant Programme and made possible my studies in the United Kingdom.

I would like to thank Professor John Simpson for being next to me in past 12 months. The comments made by Professor Simpson right at the beginning of the thesis were an invaluable resource for me. I thank Dr. Antonio Hogueane, Avelino Langa, Valera Dias, Egidio Govate, and Berino Silinto for encouraging me when needed, and for making all the effort to acquire the data used in this study.

Many people have helped me during my stay in the U.K. in too various ways to detail. My very appreciations belong to: Clare Jones, Mattias Green, Margarida Bechardas, Jose Murama, Rahma Al-Nadhiri, Shaun O'Sullivan, Stefan Kole, and Matthew Howarth.

My special thank belongs to my supervisor, Dr. Dave Bowers, who did a wonderful work on modelling the Zambezi River plumes. I am thankful to him also for his comments, wise advices, and the suggestions for my work.

Great thanks go to my parents for making every effort to provide me with the best possible education. I thank my fiancée and future wife, Yonss Jose with infinite love and patience gave me strength to survive my time in Bangor (far away from home).

At last but not least, I thank God, in all His forms, for shining the torch in the tunnel- Nothing about this would have been possible without Him.

## LIST OF FIGURES AND TABLES

| <i>Figure</i> | <i>Description</i>  | <i>Page</i> |
|---------------|---|-------------|
| 1.            | The Zambezi River delta. From the NOAA GSHHS database .....   | 3           |
| 2.            | Schematics of a river plume .....   | 11          |
| 3.            | Mid-latitude plumes classified according to the surface salinity .....  | 12          |
| 4.            | Definition diagram of a two-dimensional two-layer model .....   | 17          |
| 5.            | Model geometry .....  | 20          |
| 6.            | Model meshgrid .....  | 21          |
| 7.            | Seasonal variation of the Zambezi discharge at Tete .....   | 26          |
| 8.            | Seasonal variation of the wind speed measured at Quelimane, from 2002 to 2007 .   | 27          |
| 9.            | Simulated horizontal distribution of freshwater particles after 96 hours .....  | 28          |
| 10.           | Plume area modelled using realistic freshwater discharge (top) and windstress (bottom) conditions .....   | 31          |
| 11.           | Lagged Pearson product moment correlation coefficient between the river discharge and bulge area .....  | 32          |
| 12.           | Absorption spectra of a yellow substance sample from the Clyde Sea. Diagram from Bowers et al., (2000) .....  | 38          |
| 13.           | MODIS pseudo-colour images of red/blue nLw (top) and $k_d490$ (bottom) horizontal distribution in the vicinity of Zambezi River during July 19 <sup>th</sup> (left), 21 <sup>st</sup> (centre) and 25 <sup>th</sup> (right), 2007 ..... | 47          |
| 14.           | MODIS images of chlorophyll-a (top) and Temperature (bottom) horizontal distribution in the vicinity of Zambezi River during July 19 <sup>th</sup> (left), 21 <sup>st</sup> (centre) and 25 <sup>th</sup> (right), 2007.....            | 48          |
| 15.           | Correlation coefficient between the plume area (bounded by different red/blue nLw levels) and the river discharge (measured at Tete) at different time lags .....   | 49          |
| 16.           | Contoured map of the red/blue nLw distribution during 9 <sup>th</sup> March 2007 (i.e. the largest plume observed) .....  | 50          |
| 17.           | Size frequency distribution (%) of plume areas observed during 2002-2007 .....  | 51          |
| 18.           | Frequency distribution of runoff (left) and windstress (right) observed during 2002-2007 .....  | 52          |

| <i>Figure</i> | <i>Description</i>  | <i>Page</i> |
|---------------|---|-------------|
| 19.           | Correlation coefficient between the plume area (bounded by red/blue nL <sub>w</sub> level of 0.6, 3, and 5.5), and the river discharge (measured at Tete) at different time lags... | 52          |
| 20.           | 2-D diagram of the correlation between the freshwater plumes bounded by different levels of red/blue nL <sub>w</sub> (Y-axis) and the accumulated discharge .....                   | 54          |
| 21.           | Monthly-mean plume area (bars) and river discharge during the period 2002-2007 (line) .....   | 57          |
| 22.           | Linear relationship between the accumulated discharge and the plume area bounded by the red/blue nL <sub>w</sub> level 0.6 (top) and 5.5 (bottom) .....                             |             |
| 23.           | Monthly-mean plume area (bars) and river discharge during the period 2002-2007 (line) .....   |             |

| <i>Table</i> | <i>Description</i>   | <i>Page</i> |
|--------------|--|-------------|
| 1.           | Parameters of the numerical simulations .....  | 25          |
| 2.           | Plume characterization based on the Kelvin and Froude numbers .....  | 30          |
| 3.           | Summary of the regression and variance analyses .....  | 32          |
| 4.           | Coefficients of linear (Y=Ax+B) regression between the plume area (Y, in 10 <sup>6</sup> m <sup>2</sup> ), the accumulated river discharge (X, m <sup>3</sup> /s), and the daily river discharge (X <sub>d</sub> , in m <sup>3</sup> /s), for case-1 and case-2 plumes ..... | 51          |
| 5.           | Correlation between the windstress and the residuals of the runoff-area relation, and the results of the multiple regression (S=a +bX +cY) analysis .....  | 55          |
| 6.           | Comparison between the area-discharge linear relation obtained from model and that obtained from the satellite observations .....  | 58          |

## **CHAPTER 1**

### **INTRODUCTION**

#### **1.1. Background**

Freshwater discharges from river runoff into the ocean have an important influence on the dynamics of many coastal regions. In these regions, the freshwater buoyancy input is responsible for generating a distinct physical regime, characterized by a surface layer of less saline water flowing over the denser ambient water. With the plume being generated, a vast range of dissolved and suspended substances encounters the ocean, causing a variety of impacts, whose most severe occur within the region of freshwater influence (ROFI). These impacts include amongst others, the physical alteration of the coastline, and changes in the availability of biological resources. For better understanding these changes, an accurate description of the plume water dispersion, which is influenced by external factors (i.e. tides, winds), is of great importance.

Often, a distinction is made between plume waters, with a salinity gradient extending offshore from the river mouth, and ambient waters. Plume waters contain enhanced nutrient concentrations, due to the input of land-derived nutrients, whereas the concentration of nutrients in ambient waters is noticeably lower. According to Allen (1997), high nutrient levels can lead to enhanced phytoplankton growth and potentially to eutrophication.

The coastal waters under the influence of the Zambezi River in Mozambique are characterized by the occurrence of extensive mangrove ecosystems with high concentration of organic matter in the sediments (Mann and Lazier, 1991), making these coastal waters excellent nursery grounds for shrimp communities. The shrimp fishery is of elevated economical importance for Mozambique provided that it contributes with 15% in the total export income (Scodanibbio and Mañez, 2005). However, information regarding the effects of the Zambezi River discharges on the coastal ecosystems and their surrounding waters is scarce.

On the other hand, the size of the region encompassing the plume waters (i.e. region bounded by the ambient waters and the coastline) is often referred to as plume area, and has been reported to vary according to the river discharge. For instance, Cheng and Casulli (2004) used a three-dimensional model with unstructured grid to assess the plume dynamics over the continental shelf. The results so far, provided a comprehensive description of the salinity front position forced by different river discharges. Nezlin and colleagues (2005) used satellite imagery and examined the volume of water accumulated during episodic rainstorm events and found a strong linear relationship ( $r^2 = 85\%$ ) between the precipitated stormwater and the corresponding plume area. Although there have been several general studies on the plume dynamics, no quantitative analysis of the relationship between river plumes and its main controlling factor (the river discharge rather than the rainfall), has yet been reported. In addition, no report focusing either dimensions or dispersion patterns of the Zambezi river plume has been found in the literature.

Summarizing, the present study investigates the relationship between the freshwater discharge from the Zambezi River and the size of the corresponding plume.

## **1.2. Study site**

The Zambezi River basin covers an area of  $1.32 \times 10^6$  square kilometres in the southeast side of the African continent, draining eight countries and, it is the fourth largest basin in the continent after the Nile, Congo, and Niger basins. The climate and the rainfall within the Zambezi basin are highly variable, for instance, the climate falls in three types: semi-arid, dry sub-humid and moist sub-humid. Due to the rainfall variability resulting from the variable climate, severe droughts and dramatic floods occur periodically with considerable consequences to the surrounding communities and ecosystems.

The Zambezi is a transnational (i.e. flows across international boundaries) and an international (i.e. forms a boundary between three countries) river, which is 2750 km long. Its breadth varies from 200 to 8000 metres, and the discharge rate has a mean

value of 3000 m<sup>3</sup>/s (Gammelsrød, 1992; Scodanibbio and Mañez, 2005), ranging from 1585 to 5710 m<sup>3</sup>/s (Siddorn et al., 2001). With its origin located in Zambia, the river flows through Angola, along the borders of Namibia, Botswana, Zambia, and Zimbabwe, to Mozambique where it flows into the Indian Ocean (figure 1). The current main use of the river includes power generation, commercial fishing, hotel and tourist industry, charter vessel for tourists, and small-scale irrigation (Bourgeois et al., 2003). (Bourgeois *et al.*, 2003).

Amongst others, the course of the river is characterized by the artificial lakes impounded by dams (i.e. Kariba and Cahora Bassa), which are mostly used for power generation rather than water retention during the wet season. Despite the regulation of the river flow at the dams, the historical flood seasonality in the lower Zambezi (i.e. from the delta up to 700 km upstream) remains undisturbed, with annual floods being observed during the rainy season. However, the current maximum extent of flooded area is reported to be less than the half it was before the dams were built (Scodanibbio

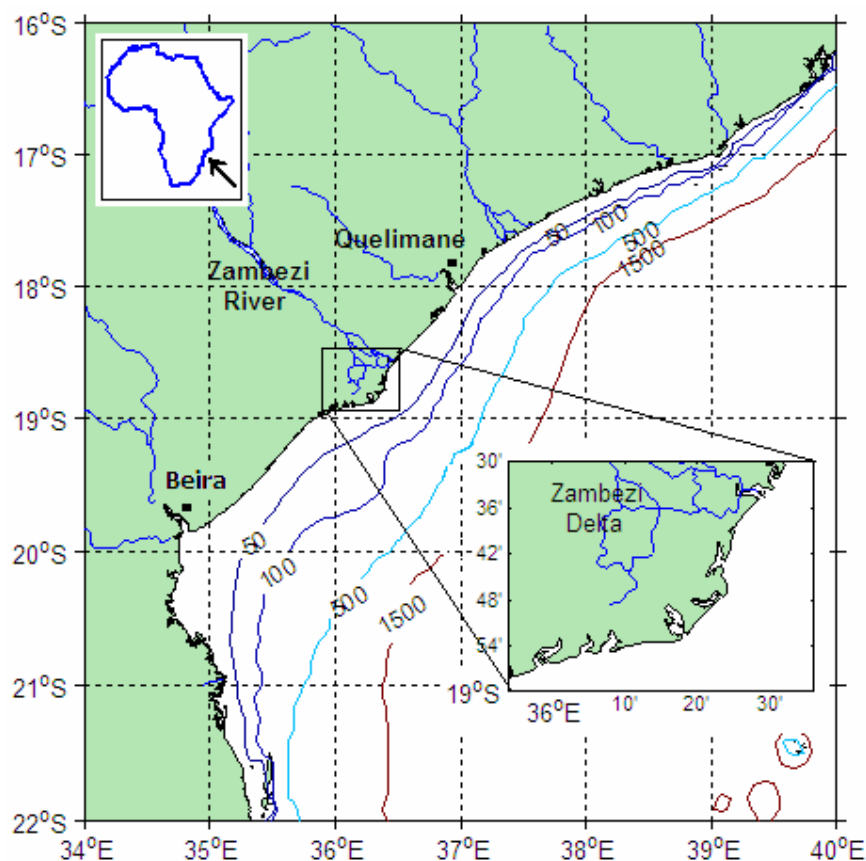


**Figure 1:** The Zambezi River delta. From the NOAA GSHHS database.

and Mañez, 2005). The rainfall variability within the basin, combined with the lack of appropriate water management policies result in a variable outflow and hence, an unpredictable river discharge into the ocean. The Zambezi River is connected to the ocean through a relatively long delta characterised by a weak navigability, due to obstruction by reeds and grasses.

The circulation in the Mozambique channel is characterized by a number of variable cyclonic eddies with a southward residual current (Sætre and Silva, 1984). Hoguane (1997) reported the speed of such currents to be approximately equal to 10 cm/s. The coastal waters exhibit a northward flow that extends up to the continental slope and to a mean depth of 1000m (DiMarco et al., 2002). Within the region of the Zambezi delta, it is believed that the flow is highly altered by the input of freshwater buoyancy, which supposedly is a potential forcing in the origin of one of the small eddies of the general circulation (Sætre and Silva, 1984). The freshwater from the Zambezi dominates the water masses in the coastal waters adjacent to the mouth, and its dynamics controls the shrimp availability in the fishing zone further north (Hoguane, 1997).

### **1.3. Objectives**

This thesis focuses on the description of the Zambezi plume dispersion patterns. The main objective of this research is to establish a relationship between the river discharge and the corresponding plume area.

In order to accomplish this goal, the following specific objectives are addressed:

- 1.** To develop a simple physics-based particle-tracking model to simulate the freshwater dispersal under realistic windstress and river discharge conditions.
- 2.** To use high-resolution satellite observations of normalized water-leaving radiance ( $nL_w$ ) to identify and hence quantify the size of the Zambezi plumes.
- 3.** To use 1 and 2 to increase insight into the relative effects of river discharge and windstress on the plume dynamics.

## **1.4. Research methodology**

In order to increase insight into the effects of windstress and river discharge on plume dynamics, the following two methods were applied to the Zambezi river plume: (i) a simulation of the plume dispersal through a numerical model, and (ii) a satellite ocean-colour based observation of the plume. In both cases, the influence of the two mentioned parameters on the plume was analysed through statistical analysis.

### **1.4.3. Numerical modelling**

In order to simulate the freshwater dispersal in the coastal region, a two-dimensional two-layer model was developed. This simple physics particle-tracking model (PTM) was coupled with a random walk component, and used to simulate the plume dispersion, under realistic river discharge and windstress conditions.

The river discharge was parameterised as discrete water particles periodically released into the river and tracked until they disappeared from the model domain. These freshwater particles were allowed to flow onto the saline water without interacting with it. By these means, neither mixing between fresh and saline water, nor the bottom drag exerted at the interface was considered in the simulations. Nevertheless, this slab model enabled us to qualitatively characterize the plume dispersion patterns and investigate the variations in the plume size.

### **1.4.4. Satellite observation**

Remotely sensed normalized water-leaving radiation ( $nL_w$ ) at two different wavelengths was used to study the plume dimensions. The radiance values were derived from the high-resolution (i.e., 1.1 km) images collected between July 7<sup>th</sup> (Julian day 188), 2002 and September 7<sup>th</sup> (Julian day 250), 2007. The sensor addressed is the Moderate Resolution Imaging Spectroradiometer (MODIS) onboard of the NASA's Aqua satellite, and its standard products include the  $nL_w$ . In order to retrieve plume dimensions, 73 pre-processed images (Level 2 LAC) were obtained from the ocean colour NASA online

archives (Mélin et al., 2007; <http://oceancolor.gsfc.nasa.gov>), and processed using *Matlab* software.

River discharge and wind speed datasets were obtained from the Mozambican National Directorate of Waters (DNA) and the Mozambican National Institute of Meteorology (INAM), respectively. The river discharge data was measured at a gauge station located 440 km from the mouth (Gammelsrød, 1992), and likewise the wind, it refers to daily values spanning the period comprised between 2002 and 2007. The referred wind speed data was collected at the Quelimane (see figure 1) meteorological station, and it has been used in combination with wind direction from historical data reported by Sætre (1985) to represent the wind effects on the plume, in the modelling exercise. The relationship between the diverse physical parameters was investigated using both *Minitab* and *Matlab* packages.

## **1.5. Outline of thesis**

The general outline of this study is as follows. Chapter 2 addresses the characterization of plumes and introduces the model. Chapter 3 focuses on the model parameterization, and the model results are presented in Chapter 4. Chapters 5 and 6 analyse the satellite images, whose results are given in the latter chapter.

Whilst the results and the analysis in Chapter 4 are based merely on the simulations of plume dispersion, Chapter 6 takes the observations into consideration and presents some comparisons between the results of both methods. Finally, the conclusions of the study are presented in Chapter 7, which also gives recommendations for future research.

## CHAPTER 2

### DYNAMICS OF A RIVER PLUME

#### 2.1. Plume characterization

The freshwater discharge from rivers generates extensive regions of significant salinity anomaly, and due to the input of momentum and buoyancy, it complicates the dynamics of the waters adjacent to the river mouth. These regions often exhibit characteristics that hugely differ either from those of the river water or from those of the ambient waters.

A typical plume pattern is one in which a layer of freshwater spreads over the ambient waters (i.e. positively buoyant). Initially, an inertial water movement takes place where the river water is projected offshore in a jet-like structure (Warrick et al., 2004). The transport in the primary direction is likely to be dominated by advection and it highly depends on the volume, timing, and intensity of the river discharge (Fong and Stacey, 2003; Nezlin et al., 2005). On the other hand, the lateral and vertical structure is dominated by dispersion and depends on the fluctuations of buoyancy and velocity in the ambient waters (Fong and Stacey, 2003). Following this jet-like motion, the plumes turn cyclonically (Southern Hemisphere) and form an alongshore buoyancy-driven current that keeps the coastline on its left-hand side.

This process is accompanied by a slow dilution of the plume, which gradually terminates as the mixing increases and the buoyancy in the far field is eroded (Warrick et al., 2004). The dominant forcing controlling the alongshore transport has been argued to be winds (Brakel, 1984; Fong et al., 1997; Manikiam et al., 1993), the buoyancy (Geyer et al., 2004; Münchow and Garvine, 1993), the coastal circulation (Warrick et al., 2007), the topography (Mestres et al., 2007), and the combination of some of these factors (Münchow and Garvine, 1993; Warrick et al., 2004).

In contrast to the surface trapped plumes, a negatively buoyant plume can be observed flowing offshore in the bottommost layer if the sediment load in the freshwater is

strong enough. According to Warrick and colleagues (2004), plumes of this type are formed by the excess density of suspended sediments and driven by gravitational forces. The suspended sediments are rapidly removed from the positively buoyant plume and transported across-shelf within the sediment-laden waters. This process occurs immediately upon discharge and within 1 km of the mouth. Measuring and analysing this type of plume involves some techniques and concepts that are beyond the scope of this study. Hence, the term *plume* refers hereafter to the positively buoyant plumes (i.e., trapped at the surface layer).

### **2.1.1. Spatial distribution of properties**

#### Salinity

Salinity represents the major difference between the riverine and coastal waters. Since the plume is a region where these waters merge, one should expect the horizontal gradient of salinity to extend offshore with the minimum value occurring at the river mouth and the maximum (or equilibrium) value occurring at the outer boundary of the plume. Warrick et al., (2007) and Siddorn (1998) have reported observations of salinity distribution of this kind for the plumes along the Southern California Bight and the Mozambican coast (i.e. near the Zambezi River). As far as salinity is concerned, the outer limit between plume water and ambient water is neither standardized nor easy to define, and for practical purposes, a particular value must be chosen from the field of observed values (Allen, 1997).

Within the plume zone, the vertical profile of salinity presents two layers, a bottom layer that is mostly comprised by ambient waters, and a surface layer consisting of less saline water. The latter is thickest immediately off the river mouth and thinned with the distance from the mouth (Warrick et al., 2005). As the turbulent processes take place, the salinity anomalies between layers tend to zero. It has been argued that the vertical salinity profile here described depends on the distance from the mouth, and on the local depth (Warrick et al., 2007).

### *Nutrients*

Large amounts of land-derived nutrients have been reported to be introduced into the sea primarily by rivers (Warrick et al., 2005), and thereafter dispersed likely between a few metres and 10s of kilometres seawards. The vertical distribution of such nutrients resembles that of salinity, where the land-derived nutrients are found in the surface waters (i.e. similar to the freshwater). Although a number of numerical simulations (Allen, 1997) and field observations (Warrick et al., 2005) suggest that the plume nutrient enrichment may lead to an increased biologic productivity, evidences of a non-linear relation have been reported. In some cases, negative consequences (i.e. algal blooms) may be influenced by excessive nutrient concentrations (Allen, 1997; Warrick et al., 2005).

### *Sediments*

As the rivers flow, they “wash” the grounds, bringing the sediments into suspension, and then carrying them to the sea. Immediately off the river mouth, two groups of sediments can be observed: i) a group composed by lighter particles that remain suspended in the positively buoyant plume, and so altering considerably the turbidity of these waters, and ii) another group composed by heavier particles that rapidly settle, and thereafter originate the negatively buoyant plume (sediment-laden waters). Therefore, the sediments in this group are transported as bedload through bottom boundary processes (Manikiam et al., 1993; Brakel, 1984; Warrick et al., 2004).

Satellite observations (Brakel, 1984) indicate that strong river discharges may generate well-defined surface plumes of suspended sediment, and the water associated with plumes of this type exhibits a high level of turbidity. The horizontal distribution of sediments within a surface plume is such that the concentration of sediments poorly correlates with salinity (Warrick et al., 2007), meaning that the suspended sediments behave non-conservatively regarding to salinity. The results so far, suggest a clear distinction between *freshwater plumes* and *sediment plumes*.

The vertical profile of sediment concentration of plume waters depends somewhat on the type of material of the seabed; however, assuming that the rivers are the unique supplier of sediments, the concentration of suspended sediment is expected to decrease with depth. Warrick and colleagues (2007) have used the beam attenuation index to assess the sediment patterns in the Southern California Bight, and they found some variability in the profiles. While a number of stations exhibited a depth-decreasing pattern, others have showed a point of minimum concentration from where, the suspended-sediments increased to a maximum value at the bottom.

#### Coloured dissolved organic matter (CDOM)

The rivers also transport considerable amounts of dissolved organic matter (DOM) into the oceans (Binding and Bowers, 2003), and as a consequence of this, one should expect these material to occur in varying levels within the plume waters (Vignudelli et al., 2004). Therefore, the organic substances carried by the plume waters can indeed be used as plume indicators. In contrary to salinity, some of these substances have been quantified using optics principles, providing further advantages to the use of remote sensing in ocean studies. Examples of organic substances successfully used in the vicinity of river mouths include the coloured dissolved organic matter (CDOM; Siddorn et al., 2001; Binding and Bowers, 2003; Odriozola et al., 2007), and the dissolved organic carbon (DOC; Del Castillo and Miller, 2008; Vignudelli et al., 2004).

The CDOM, also know as "yellow substances" or "Gelbstoff", has been found to vary linearly with salinity in the regions of freshwater influence (Bowers and Brett, 2007; Siddorn et al., 2001; Vignudelli et al., 2004). The patterns of CDOM resembles that observed for freshwater, where high concentrations are found at surface and near the river mouth (Vignudelli et al., 2004). This pattern opposes that of salinity, and this is evidenced by the negative slope in a CDOM-Salinity plot (Bowers et al., 2000; Del Castillo and Miller, 2008; Siddorn et al., 2001).

### 2.1.2. Dimensionless parameter

The dynamics of a plume is often represented by a bulge of freshwater, and a downstream coastal current, as illustrated in figure 2. According to Fong and Geyer (2002), the downstream current only carries a fraction of the discharged freshwater and the remaining fraction recirculates in a continually growing bulge. Following Garvine (1995, 1999), the general characteristics of the plume dynamics can be described by certain key non-dimensional parameters. Such parameters include the Kelvin number ( $K$ ) defined by Eq. (1), which presents a measure of the relative effect of earth rotation on the coastal current.

$$K = \frac{L}{c/f} \quad (1)$$

Where  $L$  is the cross-shore length and  $c/f$  is the baroclinic Rossby radius (internal radius of deformation).  $c$  is the internal-wave phase speed given by  $c = \sqrt{g'h}$ . With  $g'$  being the reduced gravity =  $g(\rho - \rho_0)/\rho$ ;  $h$  is the plume thickness within the bulge region,  $\rho_0$  is the density of plume waters, and  $f$  is Coriolis parameter. Plumes with  $K < 1$  behave as if the flow was non-rotating, a typical feature of small scale plumes (i.e. power plants discharges or narrow streams) at mid-latitudes or natural plume near the

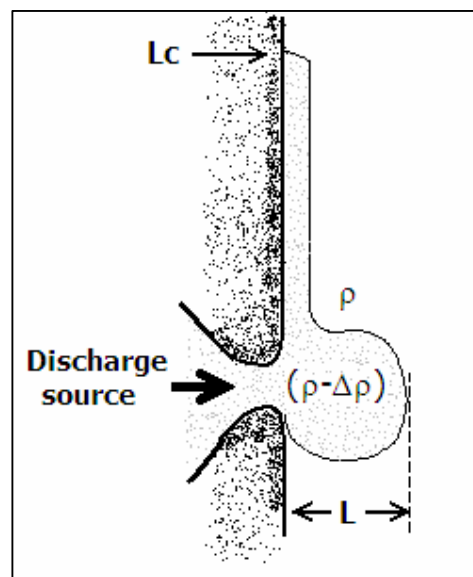


**Figure 2:** Schematics of a river plume. The across-shore ( $L$ ) and the alongshore ( $Lc$ ) extents of the freshwater are proportional to the river discharge (Cheng and Casulli, 2004).  $\rho$  is density of ambient waters.

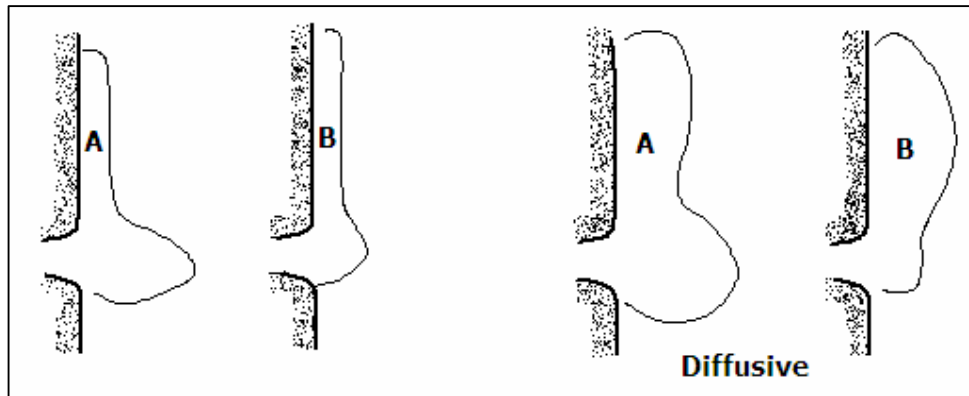


**Figure 3:** Mid-latitude plumes classified according to the surface salinity. A – supercritical plumes, B – subcritical plumes (Adapted from Chao, 1988).

equator (Garvine, 1999). In addition, plumes with  $K > 1$  are classified as “large scale discharges” and develop with the planetary rotation playing a dominant role (Garvine, 1995).

Chao (1988) suggested a classification scheme based on the Froude number ( $Fr$ ), which characterizes the shape of the plume, which in its turn, can be either supercritical ( $Fr > 1$ ) or subcritical ( $Fr < 1$ ). Figure 3 illustrates the two types of plumes. The bulge of a supercritical plume often extends considerably off the estuary mouth, and the coastal flow is often confined to a narrow jet stream. The subcritical plume has a greatly reduced bulge, whose width is comparable to that of the coastal current. These patterns complicate a little further if the plumes are of diffusive type. The Froude number is defined as the ratio  $Fr = V/c$ , where  $V$  is the near-field surface velocity of the plume (i.e. near the river mouth). Hence, this dimensionless parameter compares the input of momentum from the river to the buoyancy forcing, where the supercritical condition ( $Fr > 1$ ) implies that the near-field dynamics are strongly influenced by the river discharge (Garvine, 1995; Geyer et al., 2000).

## 2.2. Existing models

In the literature, a number of models can be found that describe the dynamics of the coastal current (Garvine, 1999), the bulge (Fong and Geyer, 2002; Nikiema et al., 2007), or both of them (Chao, 1988; Liu et al., 2008; Marsaleix et al., 1998). These

models evolved from much idealized to realistic cases (i.e. using real bathymetry and coastline). Despite the developments in three-dimensional hydrodynamics modelling achieved in the past decades, the two-dimensional (vertically averaged) models are still being used to describe situations of weak vertical stratification (Gomez-Gesteira et al., 1999), or situations of transport of solutes whose dispersion coefficients can be determined empirically (Dias et al., 2001).

The hydrodynamics models in general assume a coastal circulation governed by the following equations: the momentum equations according to Boussinesq's hypothesis (Eqs. 3 and 4), the hydrostatic pressure (Eq. 6), the volume conservation law (continuity equation, Eq. 7), and the heat and salinity conservation laws (Eq. 8). Such equations can be expressed in Cartesian frame for the Southern Hemisphere as follow (Liu et al., 2008; Nikiema et al., 2007):

$$\frac{Du}{Dt} = -\frac{1}{\rho} \frac{\partial P}{\partial x} + fv + \frac{\partial}{\partial x} \left( A_h \frac{\partial u}{\partial x} \right) + \frac{\partial}{\partial y} \left( A_h \frac{\partial u}{\partial y} \right) + \frac{\partial}{\partial z} \left( A_v \frac{\partial u}{\partial z} \right) \quad (3)$$

$$\frac{Dv}{Dt} = -\frac{1}{\rho} \frac{\partial P}{\partial y} - fu + \frac{\partial}{\partial x} \left( A_h \frac{\partial v}{\partial x} \right) + \frac{\partial}{\partial y} \left( A_h \frac{\partial v}{\partial y} \right) + \frac{\partial}{\partial z} \left( A_v \frac{\partial v}{\partial z} \right) \quad (4)$$

$$dP = -\int_z^{\eta} \rho g dz \quad (5)$$

$$\frac{\partial u}{\partial x} + \frac{\partial v}{\partial y} + \frac{\partial w}{\partial z} = 0 \quad (6)$$

$$\frac{\partial C}{\partial t} + \frac{\partial}{\partial x} \left( uC - D_h \frac{\partial C}{\partial x} \right) + \frac{\partial}{\partial y} \left( vC - D_h \frac{\partial C}{\partial y} \right) + \frac{\partial}{\partial z} \left( wC - D_v \frac{\partial C}{\partial z} \right) = 0 \quad (7)$$

Where  $D/Dt$  represents the total derivative,  $P$  is the pressure and it is given by equation 5,  $f$  is the Coriolis parameter,  $A_h$  and  $A_v$  is the horizontal and vertical eddy diffusivities, respectively.  $\eta$  is the surface elevation above a mean level  $z=0$ ,  $\rho_0$  is the freshwater density,  $\rho$  is the seawater density,  $C$  represents either the salinity or temperature. The salinity and temperature are related through an equation of state not presented here.  $D_h$  and  $D_v$  are the horizontal and vertical diffusivities, respectively.

A vast majority of plume dynamics models consider either a two-layer ocean (i.e. a surface layer of freshwater and a bottom layer of ambient waters) where the density is homogenous in each layer, or a baroclinic ocean with different treatments for the vertical direction (i.e. Cartesian coordinates, sigma coordinates). The mixing between adjacent layers is then calculated using specific turbulence closure models that produce the diffusivities in equations (3-7). In general, the mixing is a critical process in determining the dynamics and structure of the plume, given that it controls the extension of the alongshore and across-shore freshwater penetration. Garvine (1999) pointed that if the fresh and ambient waters did not mix, the extent of penetration would be unbounded with the coastal current forming a closed circuit (i.e. bounding the land mass that gave rise to the source).

Cheng and Casulli (2004) analyzed the effects of two different types of turbulence closures on the plume simulations. While one of the turbulence closure schemes considers neutral mixing coefficients (A and D in Eqs. 3-7) modified by damping functions due to stratification, the other, termed Mellor-Yamada 2.5 level and highly covered in the literature, considers the transport of the mixing length, the turbulent kinetic energy, and dissipation. They found that the former type often produced well-mixed conditions that due to the lack of analytical solutions, it could not be adjusted. Although the latter closure scheme incorporates a more complete consideration of mixing mechanisms, it was emphasized that this scheme should only be used in simulations of tidal time-scale processes.

According to de Kok (1996), the high-resolution three-dimensional models are very costly due to the long computing times involved. In addition, these models use complicated and time-consuming calibration parameters while many model parameters interact non-linearly. In one-layer models, the exchange of momentum with the bottom is neglected and so, the vertical mixing between the fresh and saline water is not an issue. These models are often applied to describe the spreading of a buoyant river plumes in the ocean with special emphasis in the arguably excellent front representation. While the thickness of the surface layer denotes the pycnocline position, the offshore extent of freshwater denotes the plume limits.

In order to avoid the artificial numerical diffusion (i.e., brought by the diffusive terms in Eq.7) in locations of sharp gradients, the hydrodynamics models are often coupled with particle tracking models (PTM; Dimou and Adams, 1993; Gomez-Gesteira et al., 1999). In the PTMs, the mass is transported as discrete particles and they successfully substitute the concentration/diffusion models (Eq. 7). The PTM have proved to be a good tool for describing processes of tracer dispersion in coastal waters, estuaries, and lagoons (Dias et al., 2001). The advantages of using a particle tracking model include amongst others, the shorter computing time (provided that only the particles where the tracer is damped are computed), and its relatively higher accuracy in describing emission spots (Dimou and Adams, 1993; Gomez-Gesteira et al., 1999).

According to Gomez-Gesteira and colleagues (1999), the displacement of water particles (or tracers) in the particle tracking models are assumed to obey the following equation:

$$\frac{dX}{dt} = U(x,t) \quad (8)$$

Where  $X$  is the tracer position and  $U$  is the velocity. The model assumes that the velocity of each component can be split into two components, where one accounts for the advective process and is obtained from a hydrodynamics model (Nikiema et al., 2007), and another component ( $U_F$ ) that accounts for the turbulent process and can be well-described by the random walk model (Dimou and Adams, 1993; Gomez-Gesteira et al., 1999). This may result in a scheme, from which the displacement is calculated as the sum of the deterministic and the small-scale random component, as shown bellow for the x-direction:

$$x(t+dt) - x(t) = U_M dt + U_F R(t) \quad (9)$$

Where  $R(t)$  is a random function with zero mean and unity standard deviation.

So far, the models have demonstrated that the properties of a river plume and the associated coastal flow can be influenced by a number of factors. These factors include the river breadth, the discharge, the exiting velocity, the degree of stratification (mixing in the vertical water column), the intensity of Coriolis acceleration (latitude of the river),

the slope of the coastal ocean, the topography, winds, and the upwelling and downwelling of coastal currents (Chao, 1988; Cheng and Casulli, 2004; de Kok, 1996; Dimou and Adams, 1993; Fong et al., 1997; Garvine, 1995; Geyer et al., 2000; Marsaleix et al., 1998; Münchow and Garvine, 1993; Nikiema et al., 2007).

A number of modelling studies have provided comprehensive and extensive results concerning the mechanisms responsible for plume formation and the dynamics within the bulge. However, only few studies have looked at the bulge dimensions (Cheng and Casulli, 2004; Nikiema et al., 2007), and they have focused on the bulge offshore extent rather than the bulge area. In addition, no hydrodynamics modelling report regarding either the relationship between river discharge and plume dimensions or the Zambezi plume itself has been found.

### **2.3. Discussion and approach**

For the calculation of plume dimensions, the velocity field near the river mouth has to be known. This chapter presented a summary of the plume characteristics, and the theoretical base of the models commonly used to simulate the freshwater dispersion was explained. In order to calculate the velocity field of a surface-trapped freshwater plume, a simple physics two-layer model was used in the current study. The choice of such a model was based on the combination of low computational costs and the need for an adequate representation of the plume limits.

The dynamics of the Zambezi plume have been previously investigated through a particle tracking model (Bowers, unpub.), the velocity field of which was obtained from a simplified (no vertical mixing was allowed) 2D hydrodynamics model. The current study constitutes an extension to the Bowers's analysis, described below.

Consider a shallow layer of rotating fluid divided into boxes having a mean depth,  $H$  and breadth,  $dx$ . The layer is bounded below by a density interface that deviates  $H$  by a small displacement,  $\eta$ , and above by a free surface (figure 4). Let each box be filled with freshwater in the form of a finite number of discrete particles with similar volume. These particles are released in a river member during the time  $dt$ , from where they

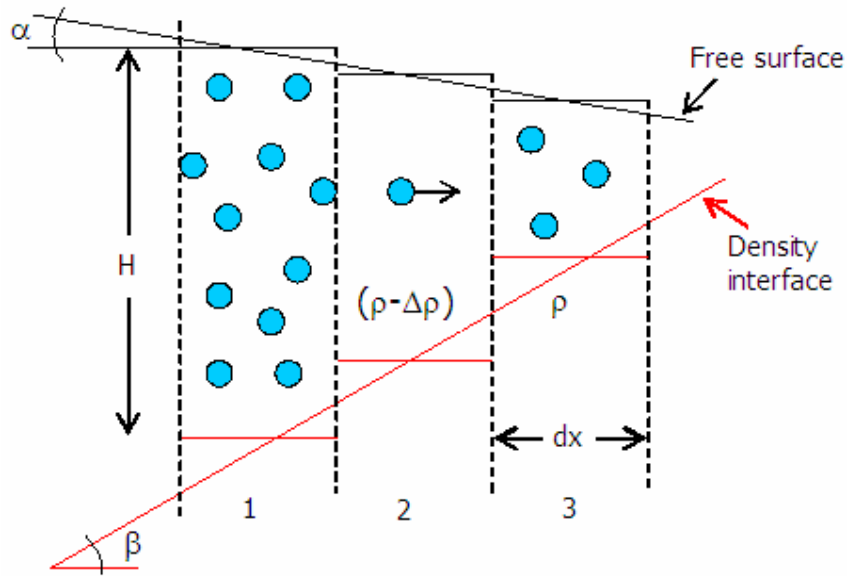


**Figure 4:** Definition diagram of a two-dimensional two-layer model.  $\alpha$  and  $\beta$  are the surface slope and the slope of the interface between plume and ambient waters, respectively. The numbers (1, 2, and 3) indicate the box or grid point.

move towards the ocean basin. Assuming no mixing and no friction between the freshwater and the saline water below it, the linearized and vertically integrated shallow water equations are:

$$\frac{D(Hu)}{Dt} = -Hg \frac{\partial \eta}{\partial x} - Hfv + \tau_{sx} \quad (11.a)$$

$$\frac{D(Hv)}{Dt} = -Hg \frac{\partial \eta}{\partial y} + Hfu + \tau_{sy} \quad (11.b)$$

Where  $\tau_{si}$  is the wind shear stress in the  $i$ -direction. The gradient term requires the movement to be from the boxes with greater to those with smaller amount of particles. The mean depth (thickness,  $H$ ) of each box is related to the number of particles ( $Np$ ) contained in the box through  $H = Vp \times Np/a$ , where  $a$  is surface area of the box, and  $Vp$  is the particle volume. So that, the surface slope can be found by taking the difference of thickness between boxes 1 and 3, in the figure 4:

$$H_1 - H_3 = \frac{Vp}{a} (Np_1 - Np_3) \quad (12)$$

From the geometry of figure 4,  $H_1 - H_3 = 2(\alpha + \beta)dx$ . Assuming the inexistence of movement in the bottom layer, we may write  $\beta = -\alpha(\rho - \Delta\rho)/\Delta\rho$ , where  $\rho - \Delta\rho = \rho_f$  is the freshwater density, and  $\alpha$  and  $\beta$  represent the free surface and the density interface slopes, respectively. Equation 12 becomes

$$\alpha \left( 1 + \frac{\rho_f}{\Delta\rho} \right) = \frac{V_p}{2dx \cdot a} (N_{p_1} - N_{p_3}) \quad (12')$$

From where the surface slope can be defined as:

$$\alpha \cong \frac{V_p}{2dx \cdot a} (N_{p_1} - N_{p_3}) \frac{\Delta\rho}{\rho_f} \quad (13)$$

So that, if the volume of each particle is known, the surface slope can be calculated and incorporated in equation 11 to derive the acceleration of each particle. Equation 13 represents an approximation for the surface slope generated by a constant discharge, where every freshwater particle has the volume  $V_p$ . However, for varying river discharges, either the number of particles released during a certain interval has to vary according to the discharge or, the number of particles remains constant and the volume of each particle has to adjust to the discharge. If the volume of each particle is known, the latter option can be implemented by substituting the term  $V_p(N_{p_1} - N_{p_3})$  in

Equation 13 by  $\left\{ \sum_i V_{1i} - \sum_j V_{3j} \right\}$ . Here the subscripts 1 and 3 indicate the grid point (i.e. a box in figure 4), subscripts i and j indicate the freshwater particles located in the corresponding grid point, and  $V$  is the particle volume given by:

$$volume = \frac{\text{runoff} \times \text{time interval for releasing}}{\text{number of particles released}}$$

By doing the mentioned substitution, the volume of freshwater in each box is computed as the sum of the volume of each water particle lying within the box. And so, the surface slope is directly related to the volume difference between consecutive boxes.

The runoff is taken as constant during the day, and the model uses a release time in the order of minutes. By these means, if four particles are released every half an hour under a runoff of  $1500 \text{ m}^3/\text{s}$ , each particle will represent  $6.75 \times 10^5 \text{ m}^3$  of freshwater.

The objective of this thesis is to develop a simple physics-based particle-tracking model to simulate the freshwater dispersal under realistic windstress and river discharge conditions. Since the mixing plays a major role in plume dispersion, we need to improve the model in order to consider the horizontal mixing processes. This can be done by adding a fluctuating-velocity term in the right-hand side of equation 11, and therefore, computing the trajectories according to equation 9. The extra term represents the random walk model.

The next chapter addresses the implementation of the model conceived in this chapter.

## CHAPTER 3

### PARAMETERISATION

#### 3.1. Introduction

The previous chapter gave the theoretical considerations for the model that is to be developed. It was pointed that the model consists of three forcings (River discharge, pressure gradient, and windstress). Besides, one extra term to account for the horizontal mixing processes is included in the momentum equation.

This chapter gives further details on the implementation of such model. It starts by describing the model domain (Section 3.2), and then the parameterization of the some model components is presented in Section 3.3.

#### 3.2. Model domain

Since this study aims to investigate the interaction between the coastal ocean and the river flow, both the coastal ocean and the connecting river have to be well represented. Figure 5 shows a plane view of the model geometry. The ocean basin is everywhere bounded by open boundaries, except the west boundary. Apart from the riverhead

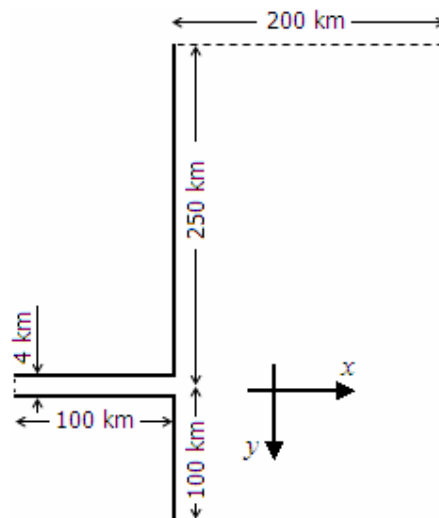


**Figure 5:** Model geometry

region, the entire west boundary is formed by a solid wall.

Initially, the ocean is filled with saline water. Freshwater is then pumped from the river member at the surface, while the saline water is withdrawn from below. In spite of this, a free surface is imposed at the top of the freshwater layer, and a rigid even surface at the interface between the two layers (i.e. a rigid lid on top of the saline water). The grid size was set to  $dx = dy = 2$  km.

### 3.3. Parameterization

The momentum equations (Eqs. 11) were discretized in an Arakawa C grid (figure 6) using the finite-difference scheme. While everywhere centred differences are applied, either forward or backward differences are applied at the solid wall boundaries. The boundary conditions are as follow. Impenetrability condition is applied at the solid walls, i.e. the velocities normal to the wall-boundary are set to zero. No mixing between fresh and saline water applies for the entire model domain.

River discharge is specified at the river upstream end as active boundary conditions via the particles introduced at a fixed time interval. The number of particles introduced corresponds to the total freshwater volume discharged during the considered time interval. By virtue of the available datasets, it is assumed that the discharge remains constant for each 24-hour period. The windstress is parameterized using the quadratic

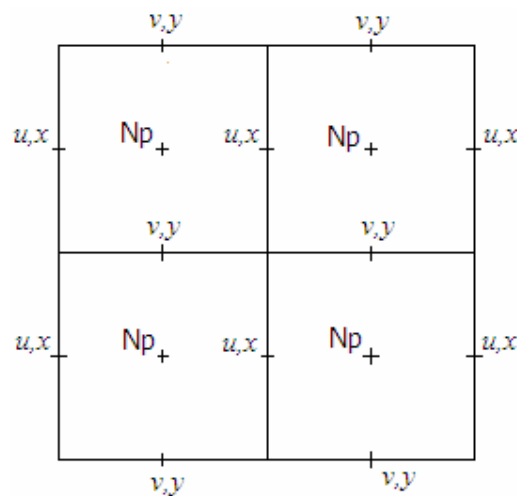


**Figure 6:** Model meshgrid

friction law, with a drag coefficient set to  $C_d = 1.3 \times 10^{-3}$  (Piñones et al., 2005), and air density  $\rho_a = 1.2 \text{ kg m}^{-3}$  (Nezlin and DiGiacomo, 2005). In analogy to the river discharge, the wind speed remains constant during the day; however, in fact daily values measured at 9 o'clock are used. Only the two most predominant wind directions are used in the computations. These correspond to the southerly winds blowing during January-September, and to the south-easterly winds blowing during October-December (Sætre, 1985).

The Coriolis parameter is set constant for the entire model domain, with a value corresponding to the latitude of the river mouth ( $18^\circ 45' \text{ S}$ ). The horizontal mixing due to the tides is parameterized as the randomly fluctuating component of velocity defined in Eq. 9, where the amplitude of the fluctuation is given by (Dimou and Adams, 1993; Sentchev and Korotenko, 2005):

$$U_F = \sqrt{2Ah \cdot \delta t}$$

Where,  $Ah = 100 \text{ m}^2/\text{s}$  is the horizontal diffusivity (Marinone et al., 2008), and  $\delta t$  is the time-step set to  $>900\text{s}$  according to the Courant-Friedrichs-Lewy (CFL) stability condition. The CFL condition requires that the information does not travel one grid point during one time step. The *Matlab* random number generator was used to generate the random function  $R(t)$  defined in Eq. 9.

Summarizing, the model computes the movement of discrete freshwater particles (introduced from the river upstream end member), the trajectories of which are calculated according to the following expressions:

$$x(t + \delta t) = x(t) + x_a(t) + Rx(t) \cdot U_F$$

$$y(t + \delta t) = y(t) + y_a(t) + Ry(t) \cdot U_F$$

Where,  $x$  and  $y$  are the zonal and meridional positions, respectively, at the time  $t$ ,  $x_a$  and  $y_a$  are the displacement obtained by integrating the velocity field  $U(u, v)$ .  $Rx$  and  $Ry$  are random numbers at the instant  $t$ .

The particles are introduced in a known position, and at each time step, the model calculates every particle's x- and y-positions at a future time ( $t+\delta t$ ). The water particles that fall within the land are placed onto the boundary and their velocity normal to the boundary are set to zero. By doing so, the impenetrability condition is implemented. For instance, within the ocean basin, the x-position of particles crossing the west boundary is set to 100 km (i.e. position of the boundary), whereas their y-position is not affected by the presence of the wall. Conversely, while the y-position of particles located within the river region is altered as the particles cross the boundary, the x-position remains unchanged.

The plume is here defined as the coastal area occupied by freshwater particles and bounded by the river mouth. This area was determined by, at each time step, counting the number of grid points containing freshwater particles, and averaging daily the resulting number of grid points. The plume thickness was taken as the sum of the height of the particles encompassed in the plume bulge.

### **3.4. Discussion**

This chapter presented the specifications of all the model parameters. The model domain was described in the Section 3.2, and the parameterization of the forcings was described in Section 3.3. Next chapter presents and discusses the model results.

Further assumptions or simplifications to the model include: (i) neglecting of the momentum transfer from the river flow to the coastal current, i.e. the advection velocity is not taken into account; (ii) omitting of the tidal and ambient current effects on the plume dynamics; (iii) neglecting the windstress effect on the hydrodynamics within the river.

The number of particles released per time interval are kept constant (i.e.  $N=4$ ) throughout the model computing time, and each particle's volume varies according to the daily runoff. In these terms, all the particles released in the same day will have the same volume. The tracking of each particle is made on the basis of the following five

quantities that constitute the "particle identity": the particle volume, the x- and y-positions, and the u- and v-velocities.

The particles that fall outside the model domain, i.e. crossing the open boundaries, are assumed to lose their identity and do not contribute to the plume anymore. The main problem of closing such boundaries is that the water particles pile up in the coastal zone and an unstable condition is reached (i.e. angle  $\alpha$  in figure 4 gets close to 90 degrees); In this situation, the amount of potential energy gradually increases and abnormal plumes can be generated (for example, plumes much larger than those expected).

The finite differencing of the pressure gradient (surface slope) term conserves mass and momentum.

This thesis focuses on the relationship between the plume area and two hydrodynamics forcings. The analysis of such relationship is made on the basis of the signal/response relation, where the signal is taken as the daily-observed river discharge and/or windstress, and the response is taken as the simulated area. The plume area is measured at each time step, and then the values are averaged daily.

According to Garvine (1999), the extent of the coastal current is strongly influenced by processes that promote the mixing between fresh and saline water. Since this model neglects the mixing with saline water, the resulting coastal current is expected to be unbounded. By these means, the northern boundary constitutes the main point from where the particles escape from the model domain. In order to avoid miscounts due to accumulation of particles at the boundary and unpredicted particle movements, only the particles located within the bulge region and 5 km from the coastline are counted in the plume area determination.

## CHAPTER 4

### NUMERICAL MODELLING

#### 4.1. Introduction

The previous chapter presented a description of the parameters considered in this model. In this chapter, the model results are presented in Section 4.2, and discussed in Section 4.3.

##### 4.1.1. Model runs

Three main model runs were considered in this study, and the settings for each run are summarized in table 1. Initially, in order to examine the model ability to simulate adequately the processes included in the model conception, a 96-hour run was performed, where alternatively each process was switched.

Secondly, four runs were performed to assess the plume characteristics under minimum and maximum river discharge for the two most predominant wind directions. In each run the river discharge and the windstress was kept constant.

Finally, one model run was performed to examine the relationship between the plume area and the river discharge (and/or the windstress). As for to the first run, realistic (varying daily) windspeed and river discharge was used in the computations of this run.

**Table 1:** Parameters of the numerical simulations. The term “varying” indicates that the respective values were updated every 24 hours, throughout the model running time. dt is the time step, and ndt is the time interval for particle releasing. “Southerly” and “south-easterly” indicate a wind blowing form the South and Southeast, respectively.

| Run | Time<br>[days] | dt<br>[min] | ndt<br>[min] | Windstress<br>[N/m <sup>2</sup> ] | Wind direction<br>[-]          | River discharge<br>[m <sup>3</sup> /s] |
|-----|----------------|-------------|--------------|-----------------------------------|--------------------------------|--|
| I   | 3              | 10          | 15           | varying                           | southerly                      | varying                                |
| II  | 15             | 10          | 15           | 5.7 x10 <sup>-1</sup>             | south-easterly or<br>southerly | 10.000                                 |
|     |                |             |              | 3.0 x10 <sup>-5</sup>             |                                | 750                                    |
|     |                |             |              | 5.7 x10 <sup>-1</sup>             |                                | 750                                    |
| III | 30             | 15          | 30           | varying                           | southerly                      | varying                                |

In order to minimize the time used by the computer to perform each run, the model time-step and the time-interval for particle releasing was appropriately changed in each of the three runs. Special care was taken to avoid contradicting the CFL stability conditions.

## 4.2. Results

### 4.2.1. Model input

#### *River Discharge*

The seasonal variation of the Zambezi River exhibits two well-defined periods: a rise season with a maximum monthly-mean discharge of  $4.0 \times 10^3 \text{ m}^3/\text{s}$  during February-March, and a fall season marked by a minimum discharge of  $1.3 \times 10^3 \text{ m}^3/\text{s}$  during September-October. However, since the building and filling of the Cahora Bassa dam (i.e. 1975), the Zambezi River discharges have changed considerably. Figure 7 presents the seasonal variations of the monthly-mean discharge, as measured at the Tete gauge station, located 115 km downstream the Cahora Bassa dam. As can be seen, the maximum discharge decreased from  $5.6 \times 10^3 \text{ m}^3/\text{s}$  (in March), before the filling of the dam to a monthly mean of  $2.9 \times 10^3 \text{ m}^3/\text{s}$  (in February), after the filling of the dam. In

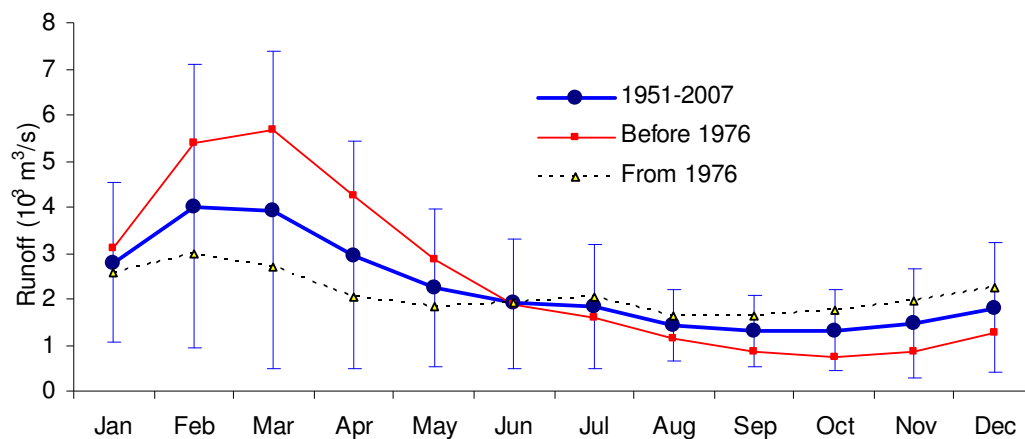


**Figure 7:** Seasonal variation of the Zambezi discharge at Tete. The error bars refer to the 1951-2007 time series, and the standard deviation (vertical lines) was calculated using the unbiased method (i.e.  $N-1$ ).

contrast, the minimum discharge has increased significantly by virtue of the regulation, for instance, it went from  $0.7 \times 10^3 \text{ m}^3/\text{s}$  (in October) before the river regulation to  $1.6 \times 10^3 \text{ m}^3/\text{s}$  (in August), after the regulation.

A comparison between the river discharges at two gauge stations, Tete and Marromeu (located further downstream), revealed that the peak in the latter station is lagged by 7 days from that of the former station. The distance between the stations is about 340 km, and the distance between the Marromeu station and the Zambezi delta is about 75 km. This leads to a mean river flow of about 0.6 m/s in that segment, which in turn means that a water particle released in Tete reaches the sea in about 8 days.

### Winds

Southerly winds constitute the dominant wind direction in the region, and they are mostly observed during January to September. The second most dominant are the southeasterly winds. During the period between October-December, the southeasterly winds become the dominant ones and the southerly winds become the second most dominant wind. Although the wind intensity is relatively low in general, it is highly variable during the year. The stronger winds are observed during September to December, and the less intense winds occur during April to July. The seasonal variation of wind speed is shown in figure 8. As can be seen, the monthly-mean wind intensity has a maximum value (4.8 m/s) in November, and a second maximum in March.

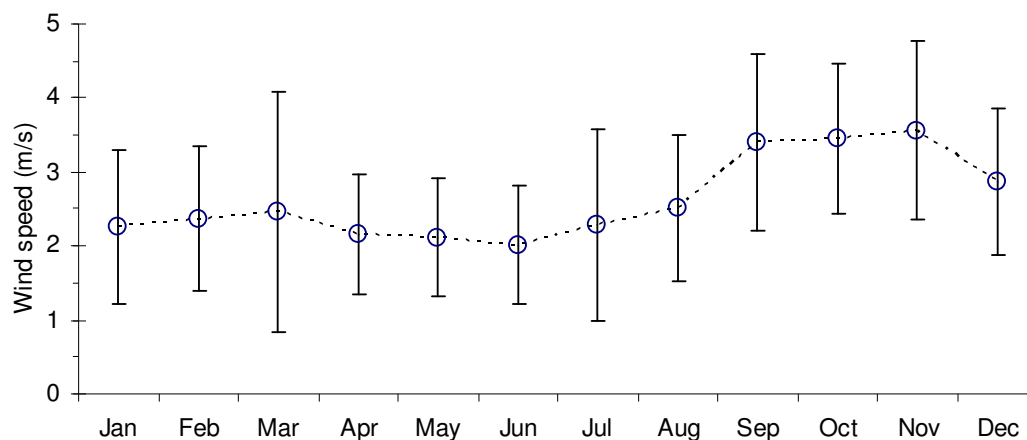


**Figure 8:** Seasonal variation of the wind speed measured at Quelimane, from 2002 to 2007.

*Hydrodynamics forcings*

The model ability to represent the different processes was investigated by alternately switching on and off selected parameters in the model runs, and then visually analyzing the modifications in the particle distribution. Figure 9 presents the particle distribution for each considered case. As can be seen in figure 9.a), the particles spread radially when the windstress and the Coriolis Effect are not considered in the computations. No

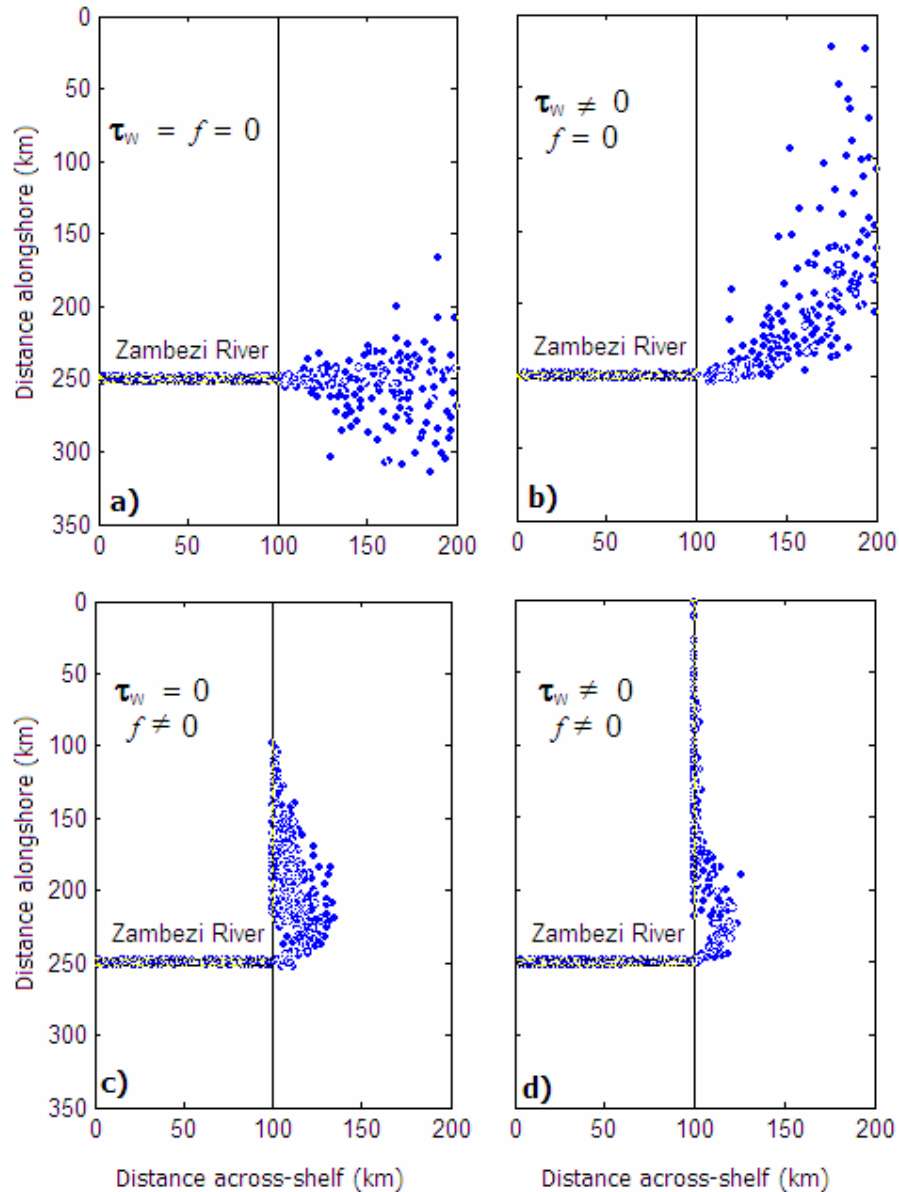


**Figure 9:** Simulated horizontal distribution of freshwater particles after 96 hours. The effect of the inclusion of either southerly winds or the Coriolis deflection in the computation is addressed. The time step is 10 minutes, and the particles were released every 15 minutes.

bulge is formed, and the average distribution of particles is roughly symmetric in relation to the position of the river mouth. When a southerly wind is added to this case (figure 9.b)), the particles are advected to the north, and similarly to the first case neither a bulge nor a coastal current is formed. In contrary, adding the Coriolis Effect instead of the windstress (figure 9.c)), the particles are deflected to the left of the river (Southern Hemisphere), and a bulge of freshwater is formed. However, the alongshore extent of the coastal current is very limited. Although this distribution of particles is fairly close to the distribution in real plumes, it is completely different from the expected distribution

Figure 9.d) presents the results for the computation with both parameters included, and it shows that a small bulge and an unlimited coastal current are formed in this situation. As it would be expected, the bulge is generated as the plume turns to the north by virtue of the Coriolis deflection, and is markedly located in the northern part of the model domain.

By comparing figure 9.c) (windstress = 0) and figure 9.d) (windstress  $\neq$  0), the influence of the windstress on the structure of the coastal currents can be visualized. When the southerly winds are acting on the plume, the coastal currents tend to be more extended to the north. Attempts to simulate other wind directions have produced movement of the freshwater particles in highly variable directions. For instance, a simulation of northerly winds (see Appendix I) produced no bulge with all freshwater particles flowing to the east direction, i.e. without changing the direction after leaving the river member, i.e. flowing at 90 degrees left of the winds.

When the windstress is applied for the whole model domain, i.e. including the river member, the freshwater particles stick together and tend to remain in the riverside (results not shown).

#### **4.2.2. Plume characterization**

The general characterization of plume dynamics was made by means of the Kelvin and Froude numbers. Table 2 presents the characteristics of plumes generated by the

**Table 2:** Plume characterization based on the Kelvin and Froude numbers. The surface velocity was estimated at a point located 5 kilometres from the coast and parallel to the river mouth. The internal wave phase speed was calculated using freshwater density,  $\rho_0 = 1000 \text{ kg m}^{-3}$ , and ambient water density,  $\rho = 1025 \text{ kg m}^{-3}$ . Wd is the wind direction.

| Wd<br>[-] | Discharge<br>[m <sup>3</sup> /s] | Windstress<br>[N/m <sup>2</sup> ] | Kelvin No.<br>[-] | Plume type  | Froude No.<br>[-] | Plume type    |
|-----------|----------------------------------|-----------------------------------|-------------------|-------------|-------------------|---------------|
| S         | 750                              | $3.0 \times 10^{-5}$              | 2.0               | Large-scale | 2.0               | Supercritical |
|           | 750                              | $5.7 \times 10^{-1}$              | 3.4               | Large-scale | 19.8              | Supercritical |
|           | 10000                            | $3.0 \times 10^{-5}$              | 1.3               | Large-scale | 8.1               | Supercritical |
|           | 10000                            | $5.7 \times 10^{-1}$              | 5.5               | Large-scale | 34.0              | Supercritical |
| SE        | 750                              | $3.0 \times 10^{-5}$              | 2.0               | Large-scale | 2.0               | Supercritical |
|           | 750                              | $5.7 \times 10^{-1}$              | 1.2               | Large-scale | 24.0              | Supercritical |
|           | 10000                            | $3.0 \times 10^{-5}$              | 1.3               | Large-scale | 8.0               | Supercritical |
|           | 10000                            | $5.7 \times 10^{-1}$              | 7.4               | Large-scale | 45.8              | Supercritical |

maximum and minimum river discharges, and influenced by the maximum and minimum windstresses (in the two most predominant directions). As can be seen, all the discharge and windstress conditions generate “large-scale” and “supercritical” plumes. The largest Kelvin and Froude numbers are generated when the river discharge and windstress are at their maximum values, for both wind directions. This indicates that at these limits, both the plume dimensions and the dynamics near the mouth are heavily influenced by the freshwater discharge. However, it is interesting to note that the smallest Kelvin number is produced under the maximum windstress conditions. This is a consequence of the fact that the southerly winds (i.e. parallel to the coast), massively contributes to the alongshore advection of the plume.

#### 4.2.3. The relationship between plume area, runoff, and/or windstress

Figure 10 presents the plume area simulated for 30 days. The realistic windstress and river discharge used to compute the plume area are plotted for comparison. As can be seen, while the trend of plume area roughly follows the observations of river runoff, it is greatly different from the trends of windstress. The trends of windstress reflect the variations occurring in the wind speed, in a time scale of few days. The correlation coefficient between the plume area and runoff is  $r=0.51$ , and that between the plume area and windstress is  $r=-0.53$ . This shows that in spite of the irregular distribution of data points in the windstress trends, it is somewhat correlated with the plume area.

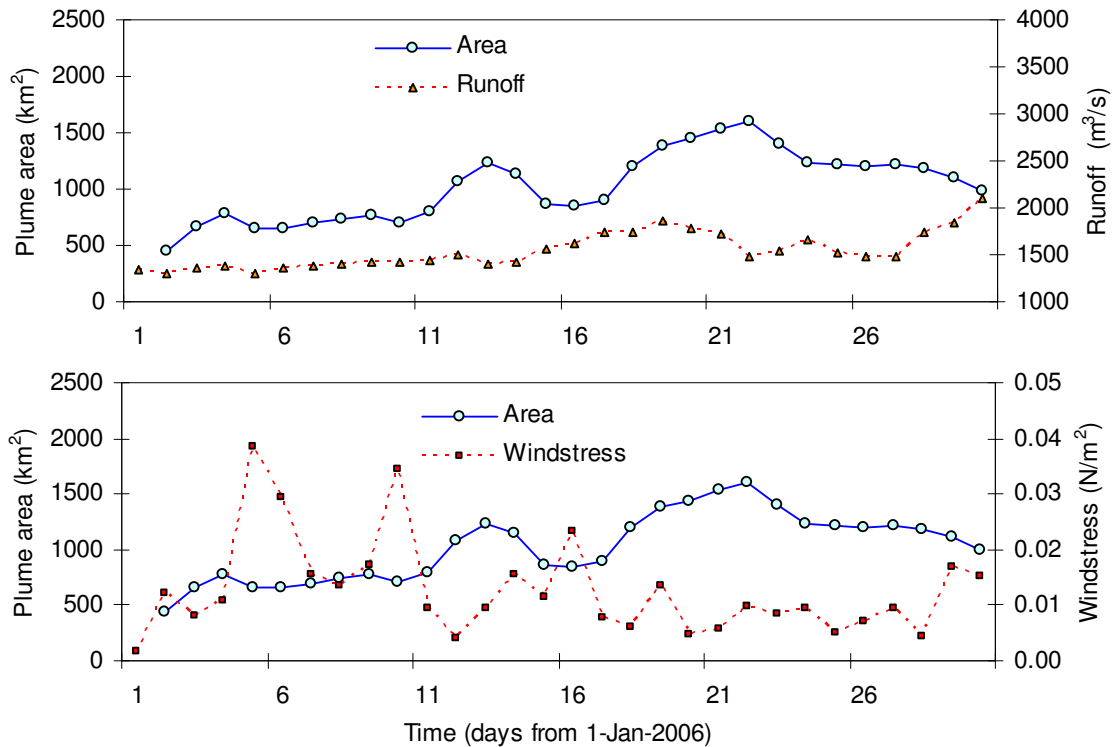


**Figure 10:** Plume area modelled using realistic freshwater discharge (top) and windstress (bottom) conditions.

The positive and negative signs of the correlation coefficient clearly indicate that, while the river discharge promotes the plume size growing, the winds promote the plume size shrinking. The latter is likely to occur through the advection of freshwater particles, such that, with the wind blowing, the freshwater particles are much rapidly dispersed (moved away from the model domain). The implication of this is the fact that strong southerly winds (i.e. the most predominant in the region), will obstruct the across-shelf dispersion of the plume.

In order to improve the correlation coefficient, the lagged Pearson product moment correlation was performed, so that, the previous day discharges could be taken into account. Figure 11 presents the variation of the correlation coefficient for different time lags. As can be seen, the plume area is better correlated with the river discharge lagged by 3 days, for which, the correlation coefficient have improved from 0.51 to 0.89. Using the river discharge lagged by 3 days and the windstress, different approximations were tested in order to find the best way to explain the plume area dependence on these parameters. Results of these tests are presented in table 3. As

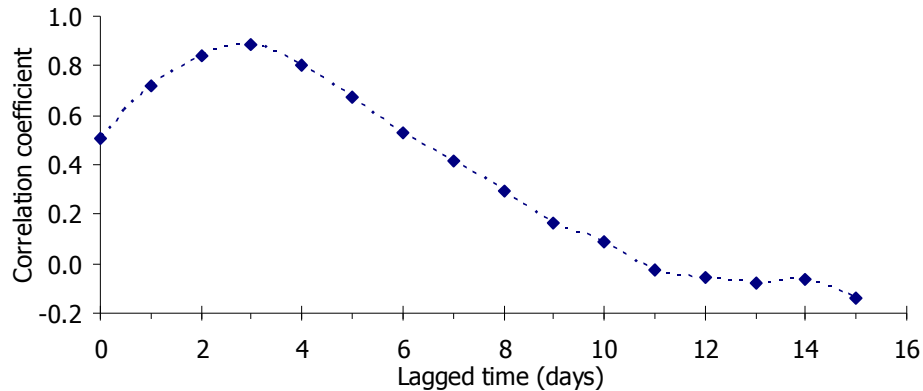


**Figure 11:** Lagged Pearson product moment correlation coefficient between the river discharge and bulge area. The time-lag is in relation to the 1<sup>st</sup> January 2006.

can be seen, the river discharge explains sufficiently the changes in plume area. In spite of this, the best explanation ( $r^2=78.2$ ) was found for linear the fit including both the river discharge and windstress. Either the case of the simple regression involving river discharge or the case of multiple regression, a considerably large negative intercept was produced, indicating that a threshold discharge does exist, below which no plume can be observed. This minimum value is  $904.0 \text{ m}^3/\text{s}$  for the simple linear regression case, and it varies between  $802.0 \text{ m}^3/\text{s}$  and  $2868.3 \text{ m}^3/\text{s}$  for the multiple regression case (taking the minimum and maximum windstresses from table 2, respectively).

**Table 3:** Summary of the regression and variance analyses.  $S$  represents the plume area (in  $10^6 \text{ m}^2$ ),  $X$  is the river discharge (in  $\text{m}^3/\text{s}$ ), and  $Y$  represents the windstress (in  $\text{N}/\text{m}^2$ ). Residuals are computed using the equation that gives the best fit.

| Parameters   | River discharge                    | Windstress           | Discharge+Windstress                         |
|--|------------------------------------|----------------------|--|
| Linear Equation  | $S = 1.73 X - 1564$                | $S = -18652Y + 1264$ | $S = 1.58X - 5728Y - 1267$                   |
| $r^2$ (%)  | 76.1                               | 28.2                 | 78.2   |
| p-value  | 0.000                              | 0.003                | 0.000  |
| Power Equation   | $S = 3.7 \cdot 10^{-6} * X^{2.66}$ | $S = 255.8Y^{-0.30}$ | $S = -2 \cdot 10^{-5} * X * 2.4 * Y^{-0.11}$ |
| $r^2$ (%)  | 68.8                               | 30.2                 | 72.1   |
| p-value  | 0.000                              | 0.02                 | 0.000  |
| Coefficient ( $r$ ) of the correlation between the residuals and the 2 <sup>nd</sup> parameter | 0.017                              | 0.753                | --   |

### 4.3. Discussion

This chapter has presented the results of the model conceived in the previous chapter, and so, it has covered two out of the three specific objectives, namely the development of a particle-tracking model, and the analysis of the effects of river discharge and windstress effects on the plume dynamics. In order to fulfil the proposed study, the next chapter introduces an approach capable of providing a more realistic picture of the plume dynamics, the remote sensing of river plumes.

#### *Plume dynamics and shapes*

Since the riverine water carries massive quantities of nutrients, sediments, organisms (which use the estuaries as nursery grounds), and many other constituents of great importance for resource managers, it becomes imperative to know the dispersion patterns of the freshwater. In its turn, these patterns depend hugely on the local factors controlling the coastal hydrodynamics, with particular emphasis to the Coriolis Effect. The classification scheme proposed by Garvine (1995), suggests that the influence of the Coriolis Effect (or the Earth rotation) on the dispersion patterns at middle latitudes can be evaluated through the non-dimensional parameter, K (Kelvin number).

The results here presented for the Zambezi river plume (18°45 S), that include both horizontal distribution of particles and an estimate of the Kelvin number, indicate that the wind drag often produces particle accelerations stronger than the surface slope does. This fact causes the plume dispersion to be highly controlled by the wind direction that acts according to the Ekman transport theory, i.e. surface water motion at 90 degrees left of the winds (Southern Hemisphere). For instance, under the two most predominant wind conditions the Zambezi plume movement was found to be northwards, generating a coastal current that remains attached to the coastline. For these conditions, the simulated Kelvin number has confirmed that, regardless the river discharge, the across-shelf plume extent is greater than the internal ratio of deformation. Meaning that, the planetary rotation plays a dominant role in the dispersion of the Zambezi plume waters.

According to the simulated Froude numbers, a bulge that extends further offshore and a coastal current of small across-shore dimensions define the shape of the Zambezi plume under the predominant wind directions. Although the model does not consider either the transfer of momentum from the river or the residual coastal currents, this plume shape is typical for coastal systems in which, the river momentum dominates the hydrodynamics. The validation of the Zambezi plume shape here presented is highly dependent on the velocity field generated by other factors (i.e. tides, ambient currents that promote the mixing between fresh and saline waters), which are likely to cause modifications to the thickness of a buoyant plume and the density field. This has implications on the plume shape because large density anomalies result in a decreased Froude number.

On the other hand, the fact that the plume area greatly correlates with the river discharge lagged by 3 days indicates that a particle released at the headwaters of the river travels with an approximated mean speed of 0.4 m/s. This value is fairly close to that estimated for the river segment lying between the two gauge stations in the lower Zambezi. This suggests that, one should expect the Froude numbers in the study region to be in the same range as those simulated by the proposed model. Therefore, field observations under weak residual coastal currents should report supercritical plumes.

#### *Relationship between plume dimensions and river discharge and/or windstress*

The plume size is one of the most important parameter for the description of plume dispersion patterns. Besides, the physical measurement of this parameter is a relatively hard task, and therefore, the determination of plume dimensions from readily measurable parameters provides added advantages. In addition, given that these readily measurable parameters include the runoff and the windstress, the relationship between these parameters and the plume size certainly is of great importance.

The plume area estimates presented in table 3, revealed that it is possible to determine the plume size with a satisfactory degree of accuracy, using measurements of river runoff and windstress. Since the approach is based on the signal/response relation, the accuracy and applicability of the plume area-river discharge relationship hugely relies

on the algorithm used to produce the signal, i.e., the model parameterization. However, it is expected that for observations of plume area, a similar relation (i.e. linear), should successfully explain its variability.

The algorithm used in this study to produce the plume signal is based on simple physics and neglects several processes, therefore, the plume area estimated by the model are likely to be excessively larger than real plume areas are. The reason for this is the fact that, the freshwater particles in the model have an unconstrained motion, while in the real coastal systems, interactions between the fresh and saline water occur from inner the estuary up to a point where these waters cannot be distinguished.

The multiple-regression involving both the river discharge and the windstress produced a linear equation that has shown to be the best approach ( $r^2=78.2$ ) for explaining the plume area variability, amongst all the approximations tested. This result is likely to have been influenced by the model geometry, since it determines the time in which a particle contributes to the plume area estimation. The reason for that is the fact that the water particles recirculate continuously within the model domain (i.e. after the bulge formation), until they reach the northern boundary where they excluded from the plume area estimation.

For the establishment of the area-runoff relation, the plume area was estimated from a 30-day simulation where the wind direction did not change. The coefficient of determination is likely to be improved if a longer time-series and therefore, other wind directions are considered in the computations.

In spite of the dominant influence played by the winds on the direction of plume dispersion, it has become clear from the regression analysis that, for plumes characterized by a bulge and a coastal flow, the river discharge rather than the windstress controls the size of the plume (taken as the bulge size). This insignificant role played by the windstress on the plume size evaluation is confirmed by the particularly slight coefficient ( $r=1.7\%$ ) of the correlation between the windstress and the residuals of the runoff-area relation. However, the comparison between the windstress and the plume area time-series has showed that in general, strong winds result in a reduced plume area, i.e. an inversely proportional relation.

The windstress effect on the plume size is likely to be considerably stronger if the freshwater is allowed to interact with ambient waters, since the winds would actively contribute to plume dilution and therefore, to a much intensified reduction of the plume area.

A dimension analysis of the regression equations, suggests that the river discharge coefficient has units [ $10^6 \text{ L}^{-1}\text{M}$ ], and the windstress coefficient has units [ $10^6 \text{ M}^{-1}\text{L}^3\text{T}^2$ ].

## CHAPTER 5

### USING SATELLITE IMAGERY TO ASSESS PLUME DIMENSIONS

#### 5.1. Introduction

The previous three chapters discussed the relationship between plume area and river discharge, and/or windstress. Using a signal simulated by a particle-tracking 2D model, the plume area dependence on the river discharge was found to be linear. In Chapter 3, the plume motion was parameterized disregarding the fact that the plumes in nature are influenced by a great number of processes. In addition, this chapter focuses on the observation of real plumes. The determination of plume dimensions is hereby discussed on the basis of satellite imagery.

First, the retrieval of salinity from satellite images of a remote location is addressed in Section 5.2. Then, the processing of satellite images focusing the plume area determination is discussed in Section 5.3. Section 5.4 discusses the overall approach and the results are presented in the following chapter.

#### 5.2. Satellite Remote sensing of salinity

Traditionally, river plumes have been assessed through tedious methods that include *in situ* measurements and relatively long field campaigns. Although these methods provide accurate and reliable results, they are expensive, time-consuming and they have a low spatial coverage. Remote sensing constitutes a much-advantaged method, since it allows for wide spatial coverage of processes, study of inaccessible areas, it gives the possibility to perform a historical assessment due to the facility of image acquisition and storing, and it has a relatively low cost when compared to *in situ* measurements. According to McKee and colleagues (2007), the lack of accuracy, the slight temporal coverage (i.e. the oldest satellite data dates as back as a few decades), and the

uncertainties due to atmospheric corrections and algorithms, are the essential disadvantages of this technology.

Salinity is a widely used parameter to assess the extension of river plumes in fieldwork; however, the salts are not optically active water components. According to Siddorn (1998), optically active components include the water itself, the suspended minerals, and the dissolved organic carbon (DOC). Where, the optically active component of DOC is termed coloured dissolved organic matter (CDOM).

The CDOM is a complex assembly of organic molecules (Stabenau and Zika, 2004) frequently found in varying concentrations in coastal waters. Based on the colour that the seawater exhibits when high concentrations of CDOM are present, its colour has been reported as being yellow-brown (Odriozola et al., 2007) and green/brown (Bowers et al., 2000). The CDOM is the dominant substance in light absorption near the river mouths and its effect become negligible in regions of high chlorophyll concentration (Del Castillo and Miller, 2008; Odriozola et al., 2007). The CDOM strongly absorbs the light in the ultraviolet and the blue end of visible spectrum, and its absorption spectra (figure 12) decreases exponentially with wavelength (Binding and Bowers, 2003; Bowers et al., 2000).

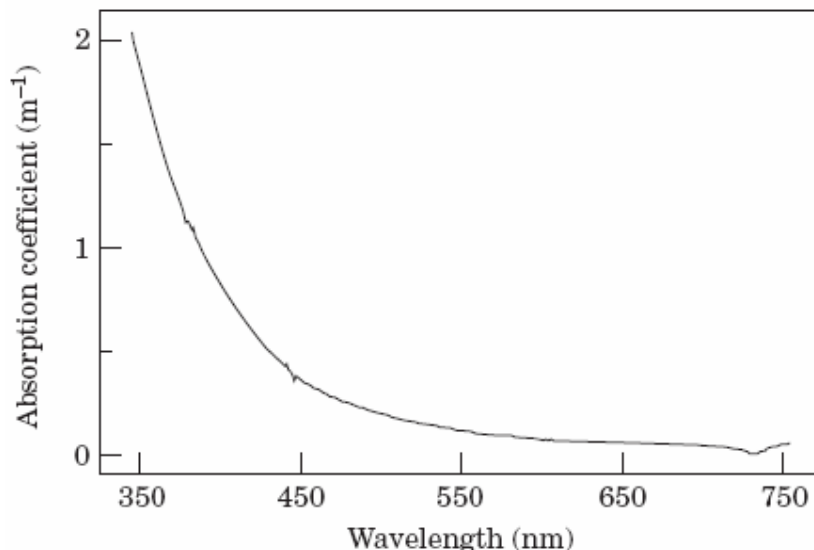


**Figure 12:** Absorption spectra of a yellow substance sample from the Clyde Sea. Diagram from Bowers et al., (2000).

The laboratorial determination of CDOM concentration often uses the spectrophotometric method and can be summarized in the following equation

$$g_{440} = 2.303(A_{440} - A_{750})/l \quad (14)$$

Where,  $g_{440}$  is the CDOM absorption coefficient/concentration,  $A_{\lambda}$  is the absorbance as measured by a spectrophotometer ( $A_{\lambda} = \log_{10}[I_0/I]$ ), and  $l$  is the pathlength in metres (Binding and Bowers, 2003; Bowers et al., 2000; Del Castillo and Miller, 2008; Siddorn, 1998; Siddorn et al., 2001). This equation actually calculates the CDOM absorption coefficient at 440nm, and then, due to their resemblance, the absorption coefficient is used as a proxy for the CDOM concentration. The absorbance at 750nm is included for the prevention of scattering by fine particles (Binding and Bowers, 2003).

Through theoretical (Bowers et al., 2000) and observational (Siddorn, 1998) work, it has been showed that the concentration of CDOM varies linearly with the red to blue reflectance ratio. For instance, Bowers and colleagues (2000) have devised the inversion technique given by equation 15, where it shows that the CDOM concentration ( $g_{440}$ ) can be retrieved from subsurface reflectance data.

$$g_{440} = c_1 \frac{R(red)}{R(blue)} - c_2 \quad (15)$$

Where,  $c_1$  and  $c_2$  are constants that depend on the absorption by water and particulate matter; and  $R$  is the subsurface reflectance. By applying this technique to the data of eight stations in the Clyde Sea, a robust correlation ( $r^2 = 0.999$ ) was found between the reflectance ratio and the CDOM. This shows that having the coefficients  $c_1$  and  $c_2$  from field data, the CDOM can be accurately estimated from the subsurface reflectances. In the same paper, Bowers and colleagues (2000) analyzed the relationship between the CDOM and salinity. They used both surface and subsurface samples and found an coefficient of determination ( $r^2$ ) of 0.99 for the straight-line fit of CDOM versus salinity ( $g_{440} = 2.88 - 0.08Sal$ ). This indicates the existence of a strong linear dependence between the CDOM and salinity, which can be written as:

$$Salinity = \alpha \cdot g_{440} + \beta \quad (16)$$

Where the slope ( $\alpha$ ) and intercept ( $\beta$ ) have to be determined from field data. Using data collected at half the Secchi disk depth in the Zambezi influenced waters, Siddorn and colleagues (2001) investigated the relation given by Eq.16 and found a good relationship between the salinity and CDOM ( $\text{Sal} = 35.7 - 16.6g_{440}$ ,  $r^2 = 76.1\%$ ), and a much stronger relation between the salinity and reflectance ratio ( $\text{Sal} = 37 - 7.07R_{555}/R_{490}$ ,  $r^2 = 90.5\%$ ). By these means, they demonstrated the correctness of the algorithm described by Eq. 16.

On the other hand, satellite imagery provides measurements of the normalized water-leaving radiance ( $nL_w$ ) rather than the subsurface radiance used in Eq. 16. The  $nL_w$  represents the radiance that would be measured exiting a flat surface of the ocean with the Sun at zenith and the atmosphere absent. Following Siddorn and colleagues (2001), the *in situ* reflectance ratio at two arbitrary wavelengths can be written as the ratio of the remotely-sensed normalized water-leaving radiances  $R(\lambda_1)/R(\lambda_2) = nL_w(\lambda_1)/nL_w(\lambda_2)$ , and hence the CDOM concentration can be retrieved from satellite data by modifying equation 15 as follow:

$$g_{440} = c_1 \frac{nL_w(\text{red})}{nL_w(\text{blue})} - c_2 \quad (17)$$

Eq. 17 shows that the concentration of CDOM in coastal waters varies linearly with the red to blue ratio of  $nL_w$ . However, in locations with high concentration of particulate matter, the coefficient  $c_2$  introduces some inaccuracies to the CDOM concentration, calculated through Eq. 17. Bowers and colleagues (2000) indicated that this unwanted effect can be lessened if the wavelength in the denominator is chosen as far towards the blue end of the spectrum (where the CDOM is the dominant absorber) as possible.

### 5.2.2. Some examples of satellite assessment of plume dimensions

Apart from CDOM, other water properties that have been used to detect river plumes include the concentration of suspended sediment, and turbidity. For instance, Nezlín and colleagues (2005) have assessed the factors that influence the incidence and dispersal of freshwater runoff in the Southern California Bight using the suspended

sediment as a plume indicator. The variations in sediment concentration due to strong rainfall were detected by using the index of backscattering by sediments, where it was used the normalized water-leaving radiance at a single wavelength,  $n_{L_w555}$ . The choice of a single wavelength as indicator of plume was based on the correlation results, which indicated strong relationship between the accumulated stormwater and the plume, and the fact that previous studies had reported a strong linear relationship between the lithogenic silica (an important constituent of riverine suspended sediment) and the  $n_{L_w555}$ . The results so far, have indicated a strong correlation between rainfall and the plume area (i.e. in perfect agreement with the clearly visible sediment plume), and by these means, suggesting that the rainfall is the primary source of plumes, in the studied site.

Despite the formidable results obtained using  $n_{L_w555}$  to detect sediment plumes, the non-linearity between the salinity and suspended sediment concentration observed by Warrick and colleagues (2007), suggests that this method might fail in detecting freshwater (or salinity) plumes. In the work done by Warrick et al. (2007), both MODIS satellite imagery and intensive field observations were used to describe the post-storm plumes in the Southern California Bight. While the suspended sediments were poorly ( $r^2=0.12$ ) correlated with salinity, the CDOM confirmed has to be a good proxy for salinity ( $r^2=0.56$ ). The results so far, revealed that once in the sea, the freshwater often detached from the coast and turned opposing the Coriolis deflection (i.e. to the left in the Southern California). The alongshore plume motion was found to be mainly influenced by local winds.

Aiming to examine the seasonal coastal movement of the suspended sediment from the Tana and Sabaki rivers in Kenya, Brakel (1984) used visible band remote sensing (Landsat, MSS band 6, 5, and 4) to map the perimeter of turbidity features. A visual inspection of the images was performed, and the turbidity plumes in scenes covering different meteorological conditions were delimited. It was found that the large turbidity plumes appear seasonally during and immediately after the two local rainy seasons. Furthermore, it was observed that despite the existence of the northward East African Coastal Current, the smaller plumes occurring in November were carried southwards

(i.e. opposing the residual currents) along the coast by the weaker northern monsoon winds.

### **5.3. Satellite image processing**

The NASA (National Aeronautics and Space Administration) online archives contain different levels of pre-processing quasi-true-colour imagery of the Earth. These archives are in constant update and as of May 2005, the Level 2 data is stored in HDF4 format files. The Level 2 files incorporate geophysical (i.e. Chlorophyll,  $n_{L_w}[\lambda]$ , Sea Surface Temperature), navigation (i.e. time and date), and flag information defined for each pixel of the scan line. The flag information is a set of 32 variables, each defining a specific source of error in the geophysical information. For each pixel, the variables can take either the value "1" meaning high possibility of contamination, or the value "0" meaning that the pixel did not meet the contamination condition. See appendix II for a complete list of contamination sources. The  $n_{L_w}$  is distributed as standard MODIS product in the following wavelengths: 412nm, 443nm, 488nm, 531nm, 551nm, and 667nm. These parameters have been previously processed for geolocation, the removing of excess data, and comparison with climatological meteorological and ozone data. In addition to the  $n_{L_w}$ , the online archive provides chlorophyll, attenuation coefficient ( $k_d490$ ), and sea surface temperature (SST) pre-processed data.

In order to apply the algorithms discussed in Section 5.2, data corresponding to the study site has to be extracted and the appropriate flags applied. By applying the flags, the bad values are removed from computation and the risk of contamination by such flag is avoided. Besides, this generates a gap in the data that has to be filled. Methods for filling the gaps include either using time (daily, weekly, or monthly) averaged values or using interpolated values for each scene. For instance, Nezhlin and DiGiacomo (2005) used a filling technique that consisted of the interpolation of grid nodes surrounding the bad value. This was applied to every bad value located  $>2$  km from the nearest "non-missing" pixel. The simplest interpolation method is likely to be the averaging of the four neighbouring pixels in a continuous manner until all the missing values have been filled.

Having the subset image containing only “good” values of  $nL_w$ , the ratio and hence CDOM (or salinity) can be calculated accurately. The plume area can then be determined by counting the number of pixels with values greater than threshold.

#### **5.4. Discussions and approach**

Obviously, the behaviour of the parameter chosen as plume indicator has to be taken into account when assessing plume dimensions through remote sensing. The conservative behaviour of CDOM regarding the salinity has become clear in the Section 5.2. Besides, the  $nL_w$  wavelength used in the denominator together with the red wavelength to form the reflectance ratio, was found to have a significant impact on the calculation of the CDOM concentration, as it was pointed in Section 5.2.

This thesis focuses on the establishment of a relationship between the freshwater discharge and the plume area using satellite observations (Chapter 5). In this chapter, the remote determination of salinity was discussed. It is worth noting that the algorithm presented to retrieve the salinity depends on the coefficients  $\alpha$  and  $\beta$ , which in turn have to be determined from field data. Although previous studies on the Zambezi influenced waters have produced the mentioned intercept and slope values, these constants cannot be used since they are likely to be time-dependent. These earlier constants would need to be tested against current field observations of salinity before they could be used.

However, checked constants were not available for this study and consequently, instead of plume area bounded by a salinity level, it is proposed a plume area bounded by a fixed level of the red to blue ratio of  $nL_w$ . By doing so, the relation area-runoff can be investigated. In summary, the use of this approach relies on the following conditions:

- The CDOM must behave conservatively at the study site, i.e. it must not be destroyed or created (Del Castillo and Miller, 2008).

- The relationship between CDOM and water flux in the river end-member must remain constant i.e. the proportion river discharge to CDOM concentration at the mouth must be constant (Del Castillo and Miller, 2008).
- The concentration of chlorophyll must be negligible, so that the light absorption in the blue end of the visible spectrum is mainly due to the CDOM.
- The Fresnel reflectance and the product of the interfacial and the irradiance reflectances are negligible (Siddorn et al., 2001).
- The CDOM must be present and in concentrations measurable from satellite sensors (Bowers et al., 2000; Del Castillo and Miller, 2008).

As for the case of salinity, the best red/blue  $n_{L_w}$  level to be used as plume indicator has to be chosen from the observed field. To fulfil this condition, firstly the plume area bounded by different ratio level has to be correlated with the river discharge, and the best correlation coefficient will define the best plume indicator. Secondly, for a river with elevated volume discharges as it is the case of the Zambezi River, the most frequent plume size has to be different from zero.

Section 5.3 has discussed the interpolation techniques used for filling the missing data after the flags have been applied to the  $n_{L_w}$  values. Although the implementation of the proposed method (averaging the four neighbouring data points) is seemingly easy and the interpolated value represents a smooth transition between the neighbouring points, the method is likely to produce inaccurate estimates in locations of strong gradients. For instance, for missing data located near the fronts, this interpolation method might cause an erroneous expansion of the front.

The most accurate method for determining the plume area includes the drawing of a contour and the calculation of the area encompassed by the contour and the coastline (i.e. the region near the river mouth). However, this method requires much longer computing times. A feasible alternative is the proposed approach, according to which, only the size of pixels containing values greater than a threshold are summed. By using this approach, data points located far beyond the reach of the plume can incorrectly be counted resulting in a less accurate plume area. The overcoming of this possible error necessarily includes a good specification of the box enclosing the plume.

## CHAPTER 6

### ANALYSIS OF SATELLITE DATA

#### 6.1. Introduction

The previous chapter discussed the measurement of the plume dimensions using satellite ocean-colour derived normalized water-leaving radiance ( $nL_w$ ) in two wavelengths. This chapter investigates the relationship between the plume area and two dynamics forcings: the river discharge and the windstress. First, details of the image processing are given in Section 6.2, and then the results are presented in Section 6.3.

#### 6.2. Methods

Seventy-three images containing at least 50% of cloud-free area near the Zambezi River were obtained for the region comprising the box bounded by 17.25°S – 20.45°S and 34.75°E – 38.50°E. The images were collected during the period between July 7<sup>th</sup> (Julian day 188), 2002 and September 7<sup>th</sup> (Julian day 250), 2007. A vast majority of the images available to us was contaminated by cloudy weather over the study site, by these means reducing the number of exploitable images to 73. The image processing was performed using *Matlab* software, and it included the removal of bad values contaminated by clouds, high satellite zenith, atmospheric correction failure, high solar zenith, and sun glint. The pixels with bad values were classified as missing-data ("MD"), and afterwards filled with interpolated (i.e. the average of the four neighbouring pixels) data. Each step of the gap-filling process added one non-missing data to the "MD" pixels located at the edges of the area covered by MD. This process was repeated until all "MD" were replaced by non-missing data.

In order to describe the characteristics of the Zambezi river plume, three images corresponding to the period 19-25 July 2007 were paired and visually analyzed. The

analysed parameters are those distributed as standard products in the Level 2 ocean-colour products (i.e. Chlorophyll, sea-surface temperature, and the diffuse attenuation coefficient).

The calculation of the reflectance ratio was based on the normalized water-leaving radiances at 667nm and 412nm (i.e. red and blue wavelengths). Each image was visually analyzed for possible influence of the freshwater coming from other rivers (i.e. located further south or north of the Zambezi). For the plumes whose limit was not clearly defined, either the image was removed from analysis or the subset area was reduced to exclude the other river's plume. The plume area was defined as the contoured area (bounded by the river mouth) covering ratio values higher than a threshold. Initially, the optimum threshold value was unknown, and in order to overcome this, ratio values within the range 0.05 – 10 were tested. Then, the ratio level bounding the plume that best correlated with the river discharge was selected as the "plume boundary" indicator.

The analysis of correlation between the plume area and either the river discharge or the windstress was based on the model of linear "signal/response" dependence between each pair of parameters. In order to evaluate quantitatively the response of the plume size to the river discharge signal, the time-lagged linear Pearson correlation coefficients were estimated. Using the area defined by the optimum plume indicator and the discharge corresponding to the lagged time, a linear regression was performed to relate these two parameters.

In order to evaluate the influence of the windstress on the plume dynamics, the residuals of the linear regression between plume area and river discharge were estimated and correlated with the windstress.

## 6.3. Results

### 6.3.1. Plume Characterization

A vast majority of the analyzed satellite images revealed that the coastal waters near the Zambezi River exhibit optical properties that largely differ from that of the surrounding waters. Figures 13 and 14 present some satellite ocean-derived quantities. These images show clearly that the plume signal is strong for the red to blue ratio of  $nL_w$ , the diffuse light attenuation coefficient ( $K_d490$ ), and the chlorophyll-a. The distribution of the red/blue  $nL_w$  reveals a pattern that reasonably resembles that of the

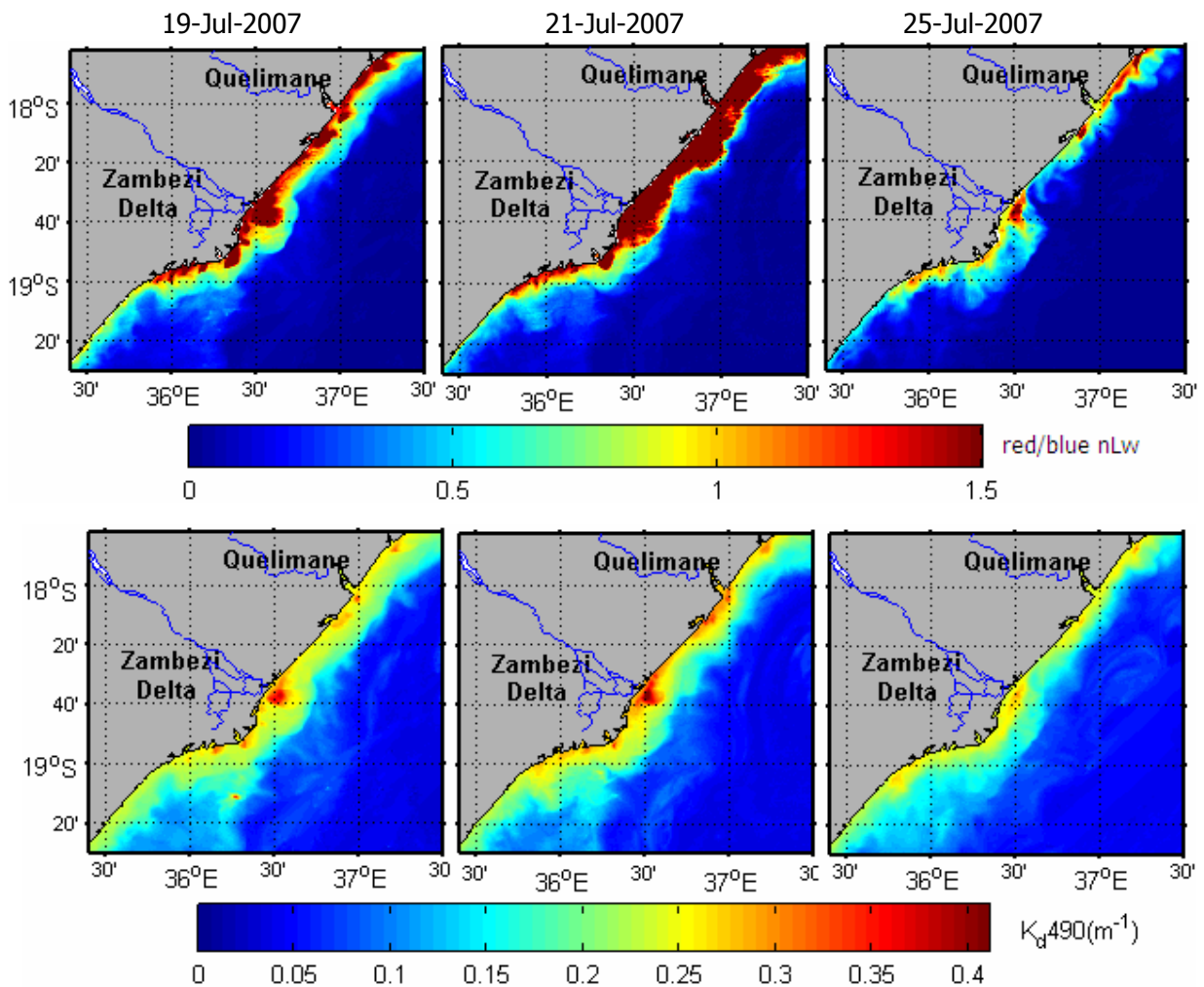


**Figure 13:** MODIS pseudo-colour images of red/blue  $nL_w$  (top) and  $k_d490$  (bottom) horizontal distribution in the vicinity of Zambezi River during July 19<sup>th</sup> (left), 21<sup>st</sup> (centre) and 25<sup>th</sup> (right), 2007.

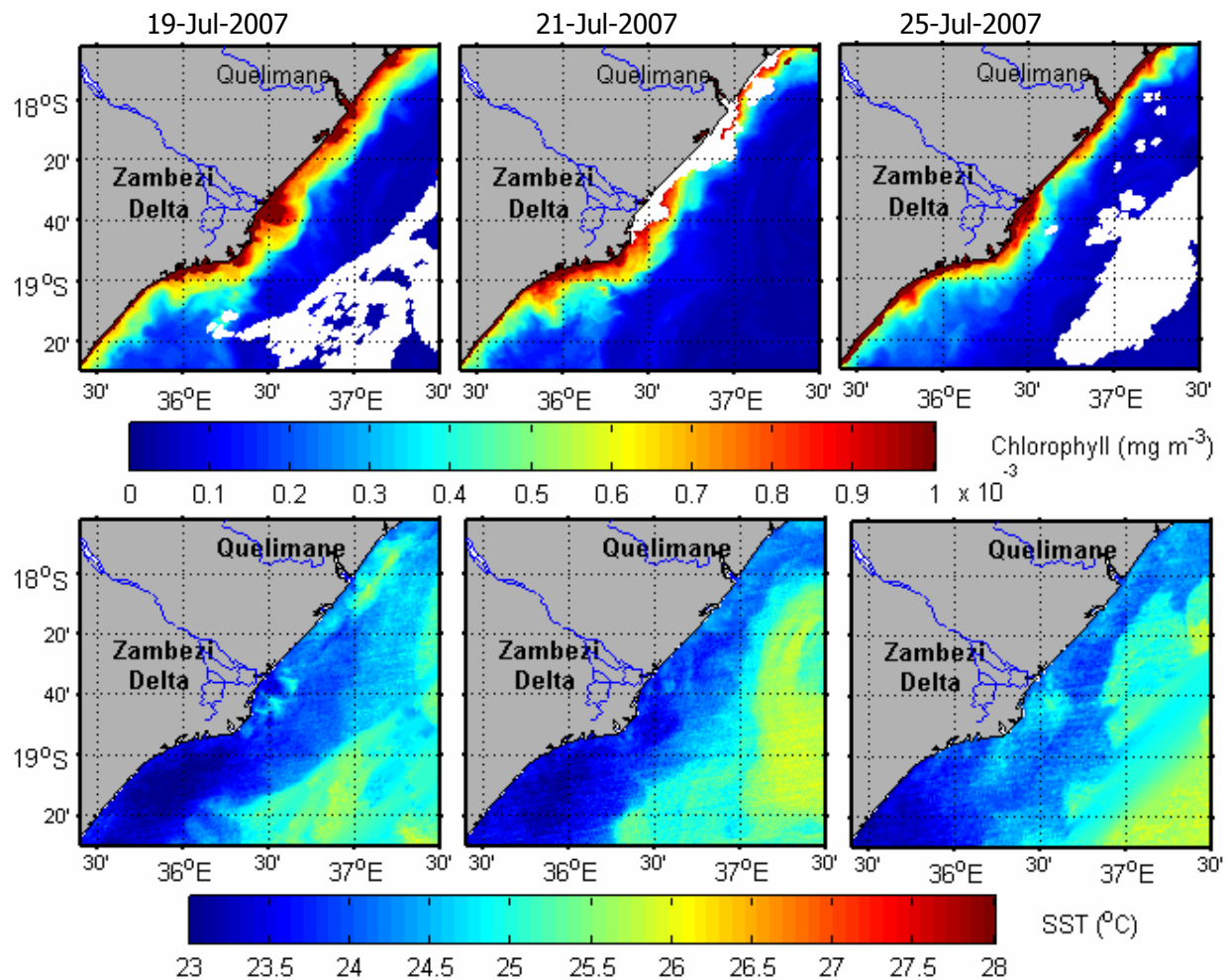


**Figure 14:** MODIS images of chlorophyll-a (top) and Temperature (bottom) horizontal distribution in the vicinity of Zambezi River during July 19 (left), 21 (centre) and 25 (right), 2007. White colours indicate that the NASA chlorophyll algorithm has failed due to cloud cover.

chlorophyll and  $k_d490$  processed by the NASA. The plume's temperature signal is considerably weak in general, and in addition, a great number of images have showed no significant variation in the temperatures of ambient and plume waters.

A bulge that extended well offshore and a moderate coastal current, as shown in the images of the red/blue reflectance (i.e. a measure of salinity) and chlorophyll, defined the plume shape in the 19<sup>th</sup> July. The image taken two days later (i.e. 21<sup>st</sup> July) shows a freshwater coastal current that developed mostly in the northern part, and has an across-shelf length comparable to that of the bulge. This feature is better depicted in

the red/blue reflectance image. A smaller plume and an almost absent coastal current characterized the 25<sup>th</sup> July images. Another important result of the satellite ocean-colour imaging is that the Zambezi freshwater does not flow northwards (through the coastal current) at all the time as commonly thought. However, in some occasions it was observed flowing southwards, or being advected offshore (image not shown) to a distance where it mixes with the ambient water and vanishes. This is likely to lead to either the plume dilution without the generation of a coastal current, or the generation of a coastal current visibly detached from the coast. The latter situation has not been observed in any of the analyzed images.

### 6.3.2. Reflectance ratio as plume indicator

The red to blue ratio of  $nL_w$  discussed in Chapter 5 was used to quantify the plume area. For each image, the area bounded by ratio levels between 0.05 and 10 (with varying steps) was correlated with the main factor regulating its size (i.e. the river discharge). The results of the correlation are presented in figure 15. Since the river discharge was measured in Tete (station located upstream the river mouth), the time-lagged Pearson product moment correlation coefficient was used to determine the time it takes the freshwater to travel all the way down to the sea, and thereafter to modify the plume size. In other words, this time lag gives an indication of the

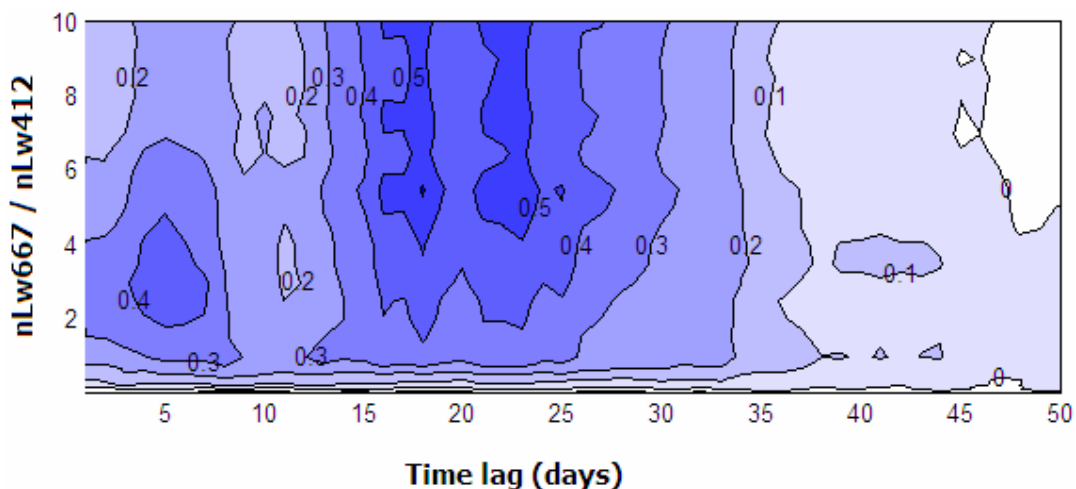


**Figure 15:** Correlation coefficient between the plume area (bounded by different red/blue  $nL_w$  levels) and the river discharge (measured at Tete) at different time lags.

discharge that best explains the plume size variability. Figure 15 reveals that the plume area bounded by ratio level 5.5 is reasonably well correlated ( $r=0.576$ ) with the river discharge lagged by 17 days. It is important noting the existence of a second maximum in the correlation coefficient occurring for the ratio level 3.0, and a lagged time of 4 days. The correlation coefficient did not improve when either ratio levels greater than 10 or time lags longer than 50 days were considered.

Figure 16 presents the horizontal distribution of red/blue  $nL_w$  levels corresponding to the maximum plume size during the period in study. The  $nL_w$  levels vary from below 0.025 in the ambient waters to more than 1.5 in the vicinity of the river mouth. Plumes bounded by ratio levels below 0.125 (i.e. more saline water) often showed to be insignificantly (negligible and negative coefficient) correlated with the river discharge, as it would be expected. This suggests that the fresher the plume water, the stronger the relation area-discharge. Conversely, the plumes that are most significantly ( $r=0.576$ )

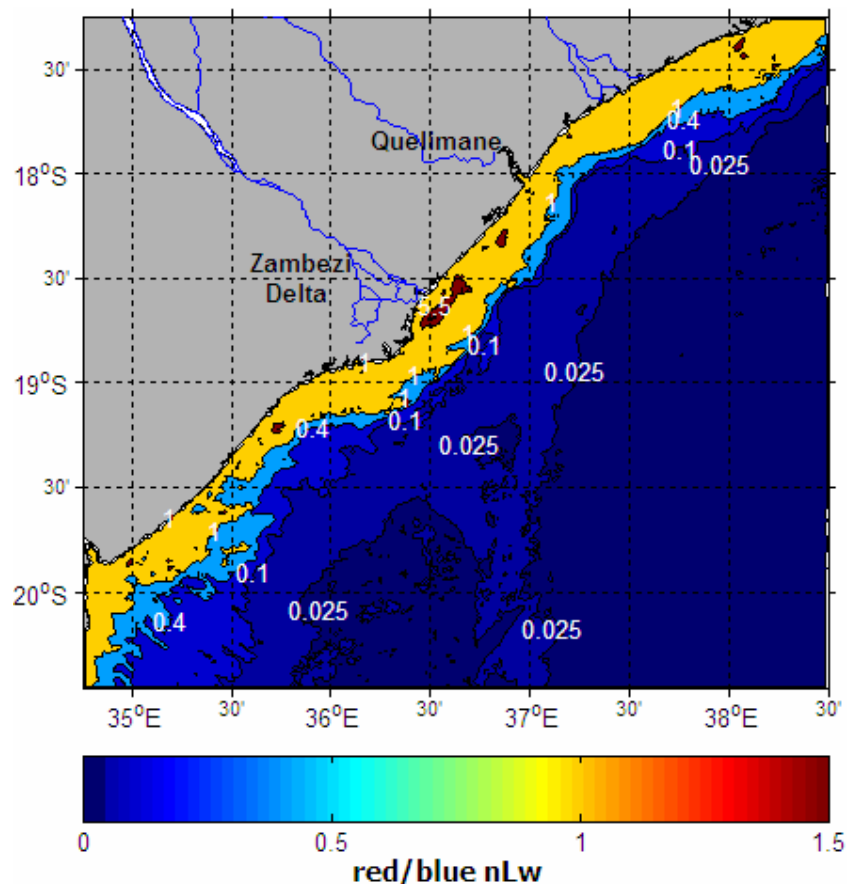


**Figure 16:** Contoured map of the red/blue  $nL_w$  distribution during 9<sup>th</sup> March 2007 (i.e. the largest plume observed).

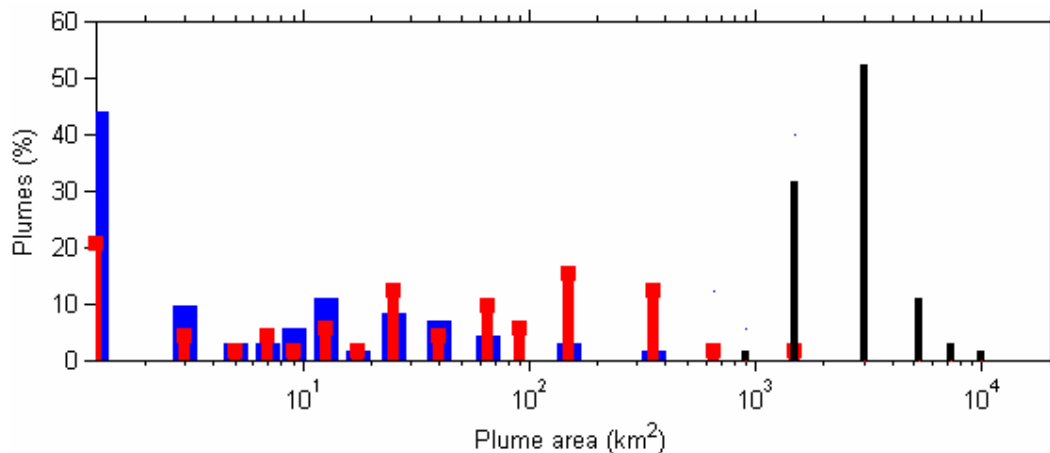


**Figure 17:** Size frequency distribution (%) of plume areas observed during 2002-2007. Blue, red, and black bars represent the areas bounded by red/blue  $nL_w$  levels 5.5, 3.0 and 0.6, respectively.

and  $r=0.475$  for the plumes bounded by  $nL_w$  level 5.5 and 3.0, respectively), correlated with river discharge, are confined to a small tongue near the mouth, and for a great number of images this area was null or considerably small.

The distribution of frequency of plume occurrence is displayed in figure 17. As can be seen, the plumes bounded by  $nL_w$  levels 5.5 and 3.0 have a bimodal and multimodal distribution, respectively, and a great number of both plumes lied within the interval 0-2  $\text{km}^2$  (i.e. no plumes were detected by satellites). Despite its relatively weak correlation coefficient, the plumes bounded by ratio level 0.6 have displayed an unimodal distribution, with the plumes having areas between 900-10.000  $\text{km}^2$ . The majority of plumes (53%) lied within the interval 2000-4000  $\text{km}^2$ , which is in a good agreement with the freshwater volume discharged by the Zambezi River (i.e. mean runoff of 3000  $\text{m}^3/\text{s}$ ). Other important features of the 0.6-bounded plume distribution is that, it is the only distribution showing an unimodal shape, and similarly to all the plumes bounded by less than 1.5 level, the areas are significantly different from zero in all images.

In addition, the frequency distributions of both the river discharge and windstress (figure 18) have showed an unimodal shape. The median discharge is about 1500  $\text{m}^3/\text{s}$  and 90% of the discharges lied within the interval 800-3200  $\text{m}^3/\text{s}$ . When this unimodal distribution of the runoff is combined with the fact that the distribution of plumes

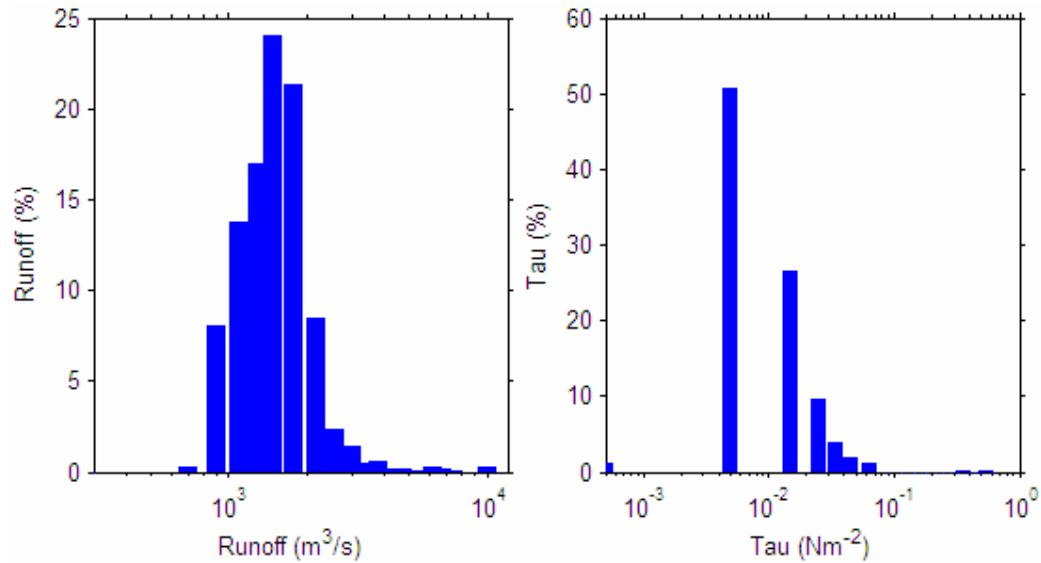


**Figure 18:** Frequency distribution of runoff (left) and windstress (right) observed during 2002-2007.

bounded by level 0.6 resembles the runoff distribution, they suggest that the level 0.6 is the best plume indicator for the far-field plumes.

In general, the correlation coefficient between the size of the plumes bounded by level 0.6 and the river discharge is somewhat variable (figure 19). However, the maximum ( $r=0.39$ ) occurs 79 days prior to the maximum discharge at the Tete gauge station.

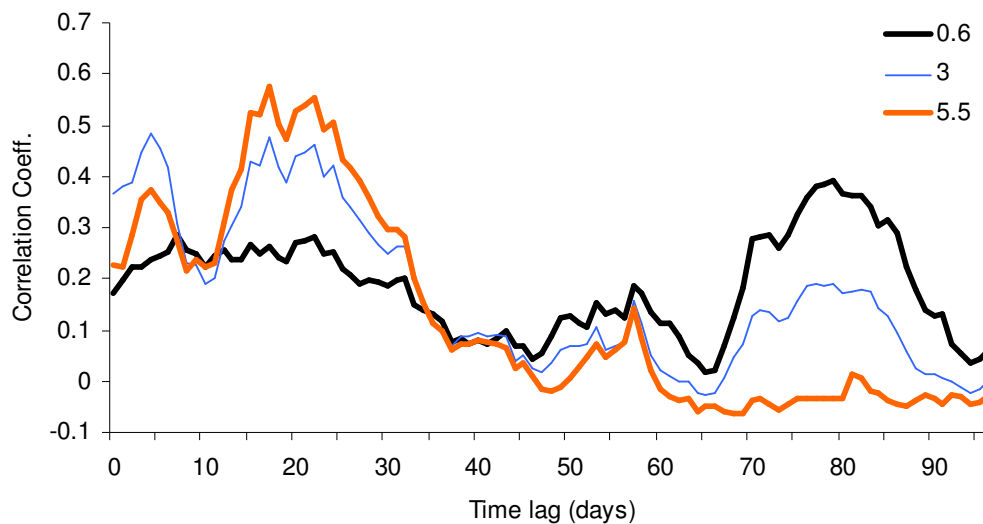


**Figure 19:** Correlation coefficient between the plume area (bounded by red/blue  $nL_w$  level of 0.6, 3, and 5.5), and the river discharge (measured at Tete) at different time lags.

The plumes bounded by level 0.6 have a second maximum ( $r=0.29$ ) in the correlation that occurs for a time lag of 7 days. In order to improve the correlation coefficient, the time-lagged river discharge was transformed according to Eq. 18 below, proposed by Nezlin et al. (2005). This transformation allows for the analysis of previous discharge effects on the  $i$ -th day plume, through the non-dimensional coefficient of persistence,  $k$ .

$$V_t = \sum_{i=1}^t k^{i-1} R_{t+1-i} = R_t + kR_{t-1} + k^2 R_{t-2} + \dots + k^{t-1} R_1 \quad (18)$$

Where  $V_t$  is the accumulated discharge (in  $\text{m}^3/\text{s}$ ),  $R_i$  is the daily river discharge in the  $i$ -th day. Nezlin et al. (2005) have defined the meaning of  $k$  ( $0 < k < 1$ ) as the  $k$ -th part of the freshwater accumulated in the preceding period and retained in the plume, implying that the  $(1-k)$ -th part of freshwater is dissipated.

The effect of the precedent discharges on the  $i$ -th day plume was tested for two cases. First, it was used the plume areas that produced the most significant correlation coefficient (i.e. bounded by the red/blue  $nL_w$  level 5.5), and the river discharge lagged by 17 days. Secondly, it was used the plume areas that produced the unimodal distribution (i.e. bounded by the red/blue  $nL_w$  level 0.6). For both cases, different numbers of preceding days ( $t$ , varying between 1 and 20) were examined and the value providing the best correlation was selected. The best number of preceding days was found to be 1, 14 and 15 for the plumes bounded by ratio level 5.5 and runoff lagged 17 days, ratio level 0.6 and runoff lagged 7 days, and ratio level 0.6 and runoff lagged 79 days, respectively. The results are displayed in figure 20.

By comparing figures 15 and 20, it can be seen that the best correlation coefficient in the case of plumes bounded by the level 5.5 have improved from  $r=0.58$  to  $r=0.75$  (figure 20.A), when the accumulated discharge was considered. This difference is quite significant and suggests a larger role played by the previous-day discharge on the plume area.

For the case of plumes bounded by level 0.6 the difference in the correlation coefficient was slight, for instance, it increased from  $r=0.29$  to  $r=0.33$  and from  $r=0.39$  to  $r=0.43$ , for the 7-day time lag (and 14 days of freshwater accumulation) and 79-day time lag

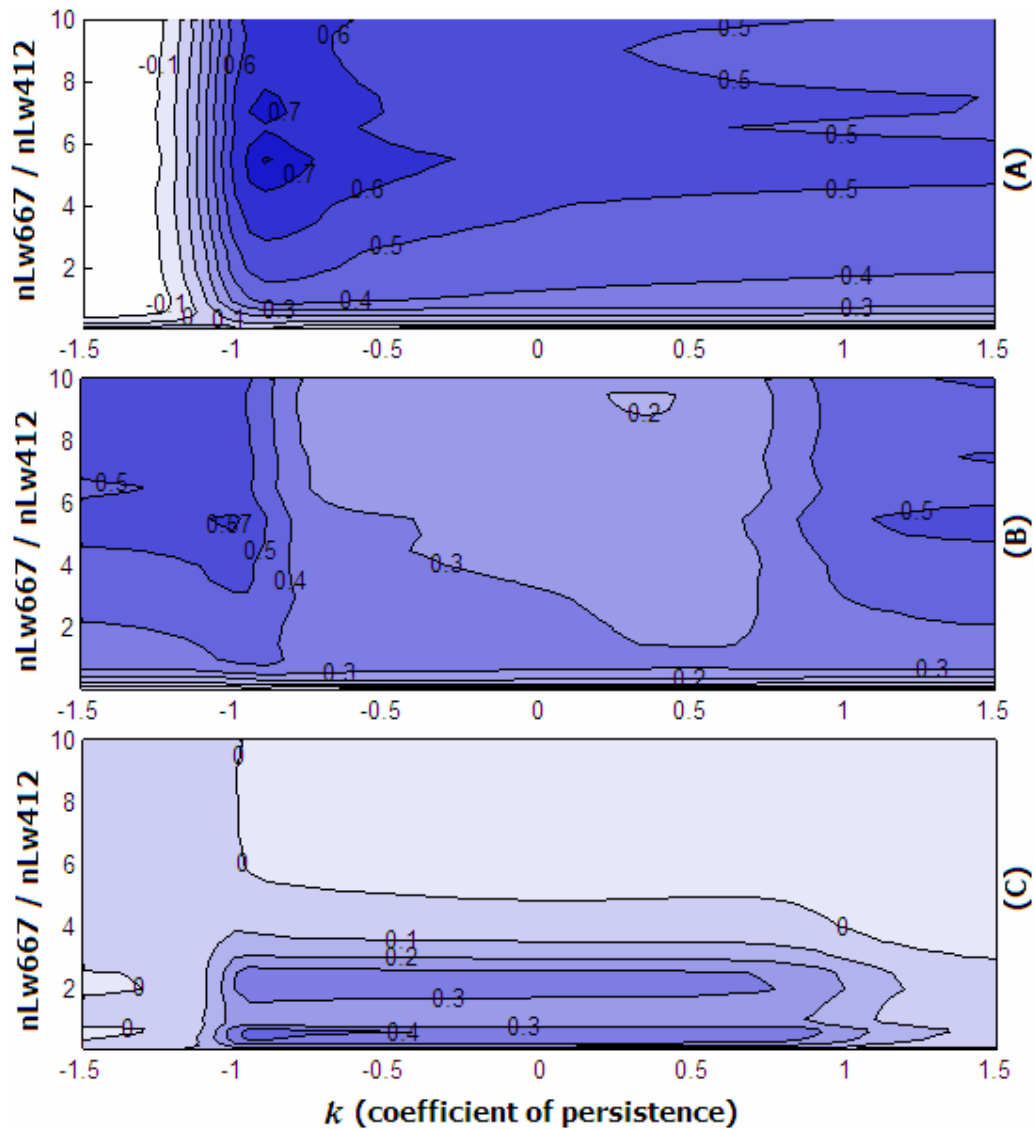


**Figure 20:** 2-D diagram of the correlation between the freshwater plumes bounded by different levels of red/blue  $nL_w$  (Y-axis) and the accumulated discharge. The accumulated discharge was estimated using different values of the coefficients of persistence ( $k$ , X-axis). For plumes bounded by  $nL_w$  level 5.5, it was used the river discharge lagged by 17 days and the discharge accumulated in the previous day (A). For the case of plumes bounded by level 0.6, it was used river discharge lagged by 7 (B) and 79 (C) days, and the discharge accumulated in previous 14 and 15 days, respectively.

(and 15 days of accumulation) cases, respectively. However, the fact that the correlation has increased, indicates that preceding day discharges in general play a certain role, and therefore they have to be considered in the plume determination.

The coefficient of persistence that produced the best correlation was found to be  $k = -0.89$ , for the case of plumes bounded by level 5.5 and discharge lagged by 17 days. For the case of plumes bounded by level 0.6, this coefficient was  $k=-0.90$  and  $k=-0.96$  for the case of the time lag equal to 7 and 79 days, respectively.

Although the time for freshwater accumulation largely differed in the two cases (i.e. one day and two weeks, for plumes bounded by level 5.5 and 0.6, respectively), the best coefficient of persistence exhibits a certain consistency.

### **6.3.3. River discharge and plume size relationship**

The previous sections attempted to select the best red/blue  $nL_w$  level to be used as the plume limit, so that the relationship between the plume area bounded by such level and the river discharge could be established. Since more than one ratio level was indicated as the plume limit, the results presented in this section will be divided into two cases, i.e. case-1 and case-2 plumes, relating the plumes bounded by ratio level 5.5 and 0.6, respectively.

Several alternatives of linear regression were attempted to allow the comparison between the use of the accumulated discharge and the daily discharge for explaining the plume area variability. The results are summarized in table 4. Since the factors that control the plume size are likely to vary seasonally, the data was analyzed regarding the time of the year, i.e. quarterly. As can be seen, in general, the plume size is better explained by the accumulated discharge rather than the daily discharge. This is showed by the coefficients of determination ( $r^2$ ) that in general are smaller for the case of daily discharge. This fact suggests a strong role played by the coefficient of persistence, whose meaning is discussed later in this chapter.

For the case-1 plumes, the linear relation runoff-area varied from robust (indicated by  $r^2=93.4\%$ ) during October-December, to insignificant ( $r^2=0.03\%$ ) during July-September. The former relation was highly influenced by the size of the sample, since only two (out of seven analysed) data points contained non-zero plume areas. The

**Table 4:** Coefficients of linear ( $Y=Ax+B$ ) regression between the plume area ( $Y$ , in  $10^6$   $m^2$ ), the accumulated river discharge ( $X$ ,  $m^3/s$ ), and the daily river discharge ( $X_d$ , in  $m^3/s$ ), for case-1 and case-2 plumes. The number of plume area data points used for regression is 73 (full dataset), 13 (Jan-mar), 24 (Apr-Jun), 29 (Jul-Sept), and 7 (Oct-Dec).

|   | Length       | Accumulated discharge |           | Daily discharge         |           |
|---|--------------|-----------------------|-----------|-------------------------|-----------|
|   |              | Linear equation       | $r^2$ (%) | Linear equation         | $r^2$ (%) |
| <b>Level 5.5</b><br>runoff lagged 17 days | Full dataset | $y = 0.14x - 6.97$    | 56.0      | $y = 0.02x_d - 19.85$   | 33.2      |
|   | Jan-Mar      | $y = 0.16x - 11.22$   | 86.9      | $y = 0.03x_d - 46.89$   | 52.2      |
|   | Apr-Jun      | $y = 0.01x + 5.07$    | 0.8       | $y = 0.005x_d - 1.08$   | 3.2       |
|   | Jul-Sept     | $y = 0.01x + 19.7$    | 0.03      | $y = 0.002x_d + 18.24$  | 0.03      |
|   | Oct-Dec      | $y = 0.16x - 20.67$   | 93.4      | $y = 0.03x_d - 38.44$   | 75.6      |
| <b>Level 0.6</b><br>runoff lagged 7 days  | Full dataset | $y = 1.48x + 1394.4$  | 10.9      | $y = 1.05x_d + 1225.8$  | 8.2       |
|   | Jan-Mar      | $y = 1.74x + 866.88$  | 41.3      | $y = 1.70x_d - 171.55$  | 32.6      |
|   | Apr-Jun      | $y = 2.11x + 1196.3$  | 5.7       | $y = 1.33x_d + 1223.1$  | 7.0       |
|   | Jul-Sept     | $y = 1.04x + 1821.8$  | 2.6       | $y = 0.51x_d + 1995.3$  | 1.6       |
|   | Oct-Dec      | $y = 0.28x + 1325.3$  | 2.8       | $y = 0.26x_d + 1180.6$  | 4.7       |
| <b>Level 0.6</b><br>runoff lagged 79 days | Full dataset | $y = 1.21x + 2211.6$  | 18.5      | $y = 0.63x_d + 1757$    | 15.5      |
|   | Jan-Mar      | $y = -1.13x + 3868.8$ | 3.8       | $y = -0.83x_d + 4667.6$ | 4.6       |
|   | Apr-Jun      | $y = 1.28x + 2314.2$  | 36.3      | $y = 0.63x_d + 1838.9$  | 24.7      |
|   | Jul-Sept     | $y = 0.31x + 2608.9$  | 0.2       | $y = 0.38x_d + 2170.3$  | 1.1       |
|   | Oct-Dec      | $y = -0.01x + 1582.2$ | 0.0       | $y = 0.27x_d + 1263.1$  | 1.6       |

second most significant ( $r^2=86.9\%$ ) relation was found for the period January-March that coincides with maxima river discharges. For all periods, the intercepts of linear equations lied between -20.7 and 19.7, and when compared to the limits of observed plume area (0–271.0  $km^2$ ), they showed to be significant and therefore, cannot be neglected.

For the case-2 plumes, the results displayed in table 2 indicate that in general the plume size is poorly correlated with both accumulated and daily river discharge, i.e., none of the linear relations can accurately explain the variability of the plumes. In spite of this, the relation area-discharge is stronger in the case of river discharge lagged by 7 days (and accumulated during the previous 14 days). This indicates that although the case-2 plumes in general (i.e. using the full dataset) correlate better with the river

discharge lagged by 79 days (figure 15), the seasonal variation can be better predicted by the discharge lagged by 7 days. Similarly to case-1 plumes, the relation runoff-area varies considerably during the year, where the best explanation ( $r^2=41.3\%$ ) for the plume variability was found for the period of maxima discharges (i.e. January-March).

By comparing the coefficient of determination ( $r^2$ ) found by using the full-length dataset to that found by using the seasonal datasets in both cases, it can be seen that the runoff-area relation is time-dependent. Moreover, the relation found using the full-length dataset misrepresents all the seasonal relations. For instance, the difference in the coefficient of determination between full-length dataset and the January-March dataset is about -30.9 and -30.4 for the case-1 and case-2 plumes, respectively. This suggests that, in the analysis of full-length dataset the runoff-area relation is massively underestimated in the period January-March, and overestimated in the remaining period. The intercept of the linear fits in the case-2 plumes were considerably large and positive numbers, with no noticeable physical significance.

The time-dependence of the runoff-area relationship has become evident from table 4, and it can be better visualized in figures 21 and 22. While the seasonal variation of the

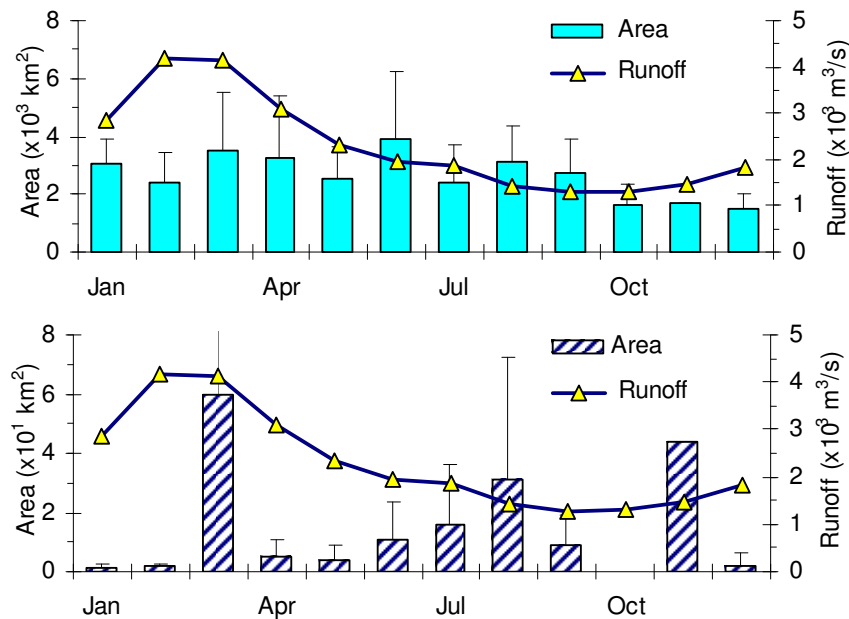


**Figure 21:** Monthly-mean plume area (bars) and river discharge during the period 2002-2007 (line). The plume area is bounded by red/blue  $nL_w$  level 0.6 (top) and 5.5 (bottom). Notice the differences in Area axis.

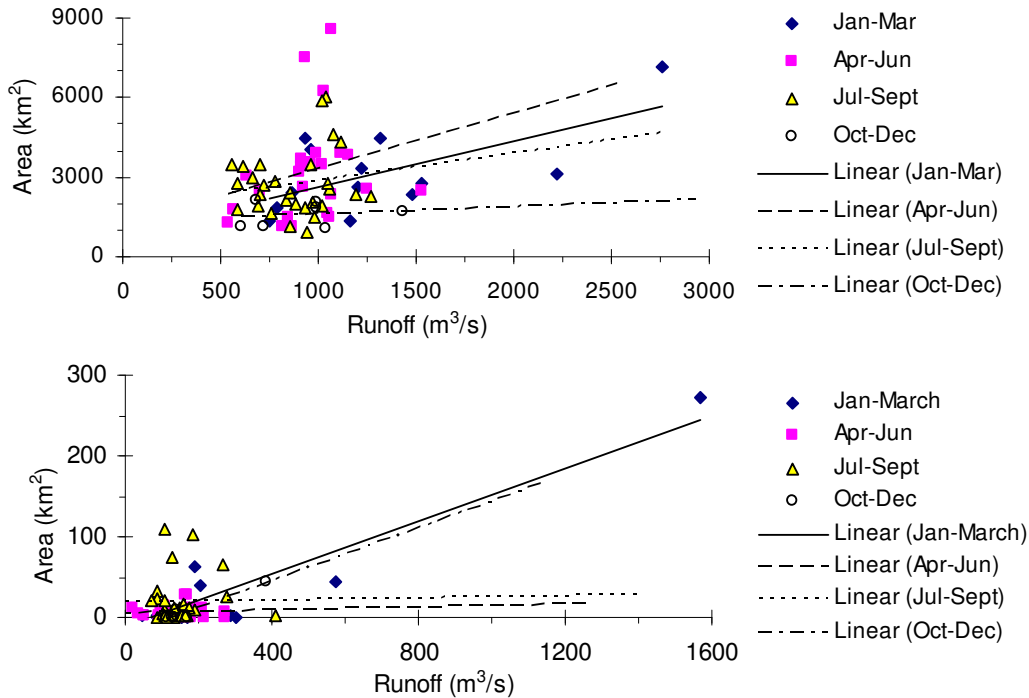


**Figure 22:** Linear relationship between the accumulated discharge and the plume area bounded by the red/blue  $nL_w$  level 0.6 (top) and 5.5 (bottom). Notice the difference in the axis scales.

river discharge has a well-defined and regular pattern, the plume area oscillates in an irregular manner throughout the year. This irregular area distribution suggests that a consistent area-discharge relation can only be found during shorter rather than the during the whole year. In addition, the timing of the maximum values of discharge and plume area reveals that the maximum plume area is lagged by at least two months from the maximum river discharge, in the case of plumes bounded by ratio level 0.6. In the case of plumes bounded by ratio level 5.5, the time-lag between the maxima is about one month.

Figure 22 is a graphical representation of the runoff-area relationship, where the regression lines were drawn following the equations presented in table 4. Although the minimum observed discharge is about 750 m<sup>3</sup>/s, the majority of data points of the case-1 plumes correspond to a river discharge less than this minimum, i.e. between 0 and 400 m<sup>3</sup>/s. This happens because the coefficient of persistence is negative and in fact, the discharges are reduced by the amount corresponding to the freshwater

dissipated in the preceding period. As can be seen, there exists a great amount of scatter of the data in general, and for the case-2 plumes (level 0.6), none of the proposed linear fits seems to be sufficient for explaining the variability of the plume size. This suggests that although the river discharge plays the dominant role in the explanation of plume dimensions, the effect of other dynamics forcings have to be taken into consideration when aiming to produce a more coherent relationship.

#### **6.3.4. Effect of Windstress**

In order to assess the contribution of windstress on the plume size variability, the residuals of the relation runoff-area were tested against the windstress using the Pearson product moment correlation coefficient. The test was conducted for the two case plumes, whereas in the case-2 plumes, only the river discharge lagged by 7 days and accumulated during 14 days was considered. For each case, two attempts were made, one considering the daily wind (i.e. the windstress of the day coinciding with plume observation), and another attempt considering the integration of windstresses during the same period the river discharge was accumulated. The results are summarized in table 5.

As can be seen for both case plumes, the residuals found using full-length dataset area insignificantly correlated with either the daily windstress or the accumulated windstress. However, the correlation involving the daily windstress have improved considerably when the shorter (seasonal) periods were considered. By these means, the area of the case-1 and case-2 plumes are adequately correlated ( $r=0.5$  and  $0.75$ ) with the daily windstress in the period April-June and October-December, respectively.

In terms of the physical meaning, the accumulated windstress seems to be more appropriate for explaining the variability of the residuals of area-discharge relation, for two reasons. First, it has become clear that plumes are influenced by the river discharges prior to plume observation, and so, it is seemingly correct to take into account the effect that the wind had on these previous discharges. Secondly, the energy transferred (from the winds to the ocean) at any particular time hardly reflects

**Table 5:** Correlation between the windstress and the residuals of the runoff-area relation, and the results of the multiple regression ( $S=a +bX +cY$ ) analysis.  $r_x^2$  is the coefficient of determination of plume area using the river discharge only, and is placed here for comparison purposes.  $r_1$  is the correlation coefficient involving the daily windstress,  $r_2$  represents the case involving the accumulated windstress.  $S$  is the plume area (in  $10^6 \text{ m}^2$ ),  $X$  is the accumulated river discharge (in  $\text{m}^3/\text{s}$ ), and  $Y$  is accumulated windstress ( $\text{N}/\text{m}^2$ ).  $r_{xy}^2$  is the coefficient of determination of plume area,  $S$ . The number of data points used for regression is 73 (full dataset), 13 (Jan-Mar), 24 (Apr-Jun), 29 (Jul-Sept), and 7 (Oct-Dec).

|   | Length       | Correlation coefficient |       |       | Multiple regression     |                |
|---|--------------|-------------------------|-------|-------|-------------------------|----------------|
|   |              | $r_x^2$ (%)             | $r_1$ | $r_2$ | Linear equation         | $r_{xy}^2$ (%) |
| <b>Level 5.5</b><br>runoff lagged 17 days | Full dataset | 56.0                    | 0.11  | 0.15  | $S= -13.3 +0.149X+213Y$ | 60.3           |
|   | Jan-Mar      | 86.9                    | 0.05  | 0.002 | $S= -11.3 +0.163X +3Y$  | 86.9           |
|   | Apr-Jun      | 0.8                     | 0.50  | 0.31  | $S= -0.63 +0.012X+277Y$ | 10.4           |
|   | Jul-Sept     | 0.03                    | 0.20  | 0.30  | $S= 1.7 +0.071X +318 Y$ | 10.9           |
|   | Oct-Dec      | 93.4                    | 0.27  | 0.38  | $S= -25.4 +0.170X +68Y$ | 94.4           |
| <b>Level 0.6</b><br>runoff lagged 7 days  | Full dataset | 10.9                    | 0.12  | -0.19 | $S= 2116 + 1.35X -293Y$ | 14.5           |
|   | Jan-Mar      | 41.3                    | 0.01  | -0.17 | $S= 1355 + 1.75X -270Y$ | 43.0           |
|   | Apr-Jun      | 5.7                     | 0.45  | -0.14 | $S= 3757 + 0.90X -955Y$ | 8.7            |
|   | Jul-Sept     | 2.6                     | 0.30  | 0.14  | $S= 512 + 1.99X +260Y$  | 7.4            |
|   | Oct-Dec      | 2.8                     | 0.75  | -0.16 | $S= 1808 + 0.157X -98Y$ | 5.8            |

the total amount transferred since the plume was generated. These facts suggest that although the correlation involving the daily windstress is much stronger, that involving the accumulated windstress is more meaningful.

It is interesting to note that for all the cases analysed, the plumes observed during January-March, are amongst all the plumes better correlated (i.e.  $r^2= 86.9\%$  and  $41.3\%$ ) with the river discharge. In contrast, their residuals are amongst all, the least correlated with the windstress. This suggests that in general, when the river discharges are at their maximum, the plume size is predominantly influenced by the discharge, and the effect of winds is negligible.

By comparing the effect of the accumulated windstress in the two cases illustrated in table 5, it can be seen that, the influence of windstress during the year is stronger for

the case-1 plumes, except during the period January-March when it is stronger for the case-2 plumes.

Table 5 also shows that when the regression is performed having the windstress and the river discharge together as predictors, the resulting relation is slightly better. In spite of this improvement, for a vast majority of the cases (i.e. the seasonal relations) the relation remains insignificant, i.e. with a coefficient of determination  $r^2 > 50\%$ . This suggests that factors other than the river discharge and windstress (i.e. not addressed in this study) might play a considerable role in the plume variability.

As shown in figure 23, the trends of the monthly-mean windstress oppose those of the

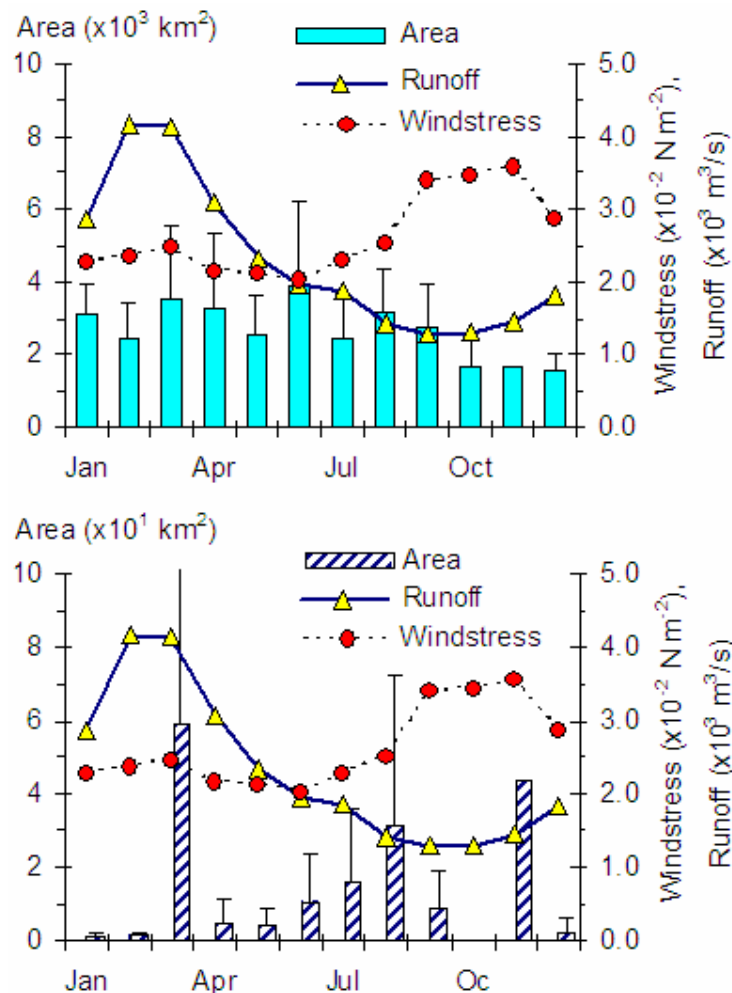


**Figure 23:** Monthly-mean plume area (bars) and river discharge during the period 2002-2007 (line). The plume area is bounded by red/blue  $nL_w$  level 0.6 (left) and 5.5 (right). Notice the difference in the plume area axis scales.

river discharge. While the minima windstresses and maxima discharges occur in the first half of the year, the second half is marked by maxima windstresses and minima discharges. This distribution is conducive to an “equilibrium” situation around June that coincides with the maximum in the plume size, for the case-2 plumes.

The size of the case-1 plumes exhibits an irregular distribution, in relation to the distribution of windstress and discharge, all throughout the year. However, two distinct features are evident in figure 23. First, the maximum plume area coincides with maxima river discharge. Secondly, the second maximum plume area coincides with maximum windstress. This indicates that in contrary to what happens with the case-2 plumes, strong winds are capable of creating large differences in the size of the case-1 plumes, mirroring the correlation found between these plumes and the seasonal accumulated windstress.

### 6.3.5. Comparison with model results

Since the model was run for 30 days starting at the 1<sup>st</sup> of January 2006, the model results were compared with the plumes observed during the period January-March. Table 6 presents the main findings in both studies and the error estimates. As can be seen, the model reproduces fairly well the slope of the area-discharge relation, for the case-2 plumes. However, it drastically fails to reproduce the intercept of such relation. Despite the discrepancies found in the intercept, the correlation involving the windstress has showed some consistency. In fact, the residuals poorly correlated with the windstress either using simulated plumes or using observed plumes.

**Table 6:** Comparison between the area-discharge linear relation obtained from the model and that obtained from the satellite observations. Error is calculated according to:  $(X_{Obs}-X_{Mod})/X_{Obs}$ .

|  | Model | Observation |        | Error (%) |        |
|--|-------|-------------|--------|-----------|--------|
|  |       | Case-1      | Case-2 | Case-1    | Case-2 |
| Slope (s/m)  | 1.73  | 0.16        | 1.74   | -981      | 0.57   |
| Intercept ( $10^6$ m <sup>2</sup> )                  | -1564 | -11.22      | +867   | -13839    | 280.76 |
| Coefficient of determination ( $r^2$ , %)            | 76.1  | 86.9        | 41.3   | -         | -      |
| Correlation between the residuals and the windstress | 0.02  | 0.05        | 0.01   | -         | -      |

## 6.4. Discussion

### 6.4.1. Plume assessed by satellite imagery

This chapter presented the results of the approach described in the Chapter 5, which aimed at the establishing of a relationship between the plume area and the river discharge, based on the salinity (or CDOM) signal evaluated in terms of the red to blue ratio of normalized water-leaving radiance.

Despite the existence of a maximum ( $r=0.58$ ) in the correlation between the area and discharge, the identification of a ratio level to be used as plume indicator was not simple. First, the location of this maximum correlation was not evident in a contour plot, since a great number of neighbouring data points have exhibited values very close to this maximum. Besides, the plot has presented more than one maximum, occurring for different levels of reflectance ratio, and at different time lags. Secondly, the localization of the case-1 plumes (i.e. those that have produced the highest correlation) in a map of the study region, did not reflect the volume of freshwater discharged by the Zambezi River.

Based on the correlation tests and the analysis of frequency distribution, two regions presenting different characteristics could be distinguished within the plume waters: a near field marked by the ratio level 5.5 and a far field marked by the ratio 0.6. By these means, two (instead of one) ratio levels were identified as being the plume limits, and consequently, two types of plumes were analysed. The near-field plumes were characterized by a strong influence of both river discharge and windstress, while the far-field plumes were characterized by a relatively weaker influence of both river discharge and windstress.

The use of accumulated discharge rather than the daily discharge showed to be a much stronger approach for explaining the plume area variability. This approach has revealed that, in contrary to the positive coefficient of persistence found by Nezlin and colleagues (2005) in stormwater plumes, the Zambezi river plumes have a negative coefficient that varies between  $k=-0.90$  to  $k=-0.89$ . According to the definition of this

coefficient, a negative coefficient would require that only a portion of the excess discharge in subsequent days are used to increase the plume size. The remaining discharge would be used to replace the freshwater diluted in the preceding days. By these means, a coefficient of persistence  $k=-0.90$  means that 90% of the discharged freshwater volume is either diluted or advected everyday.

The linear relation between the plume area, the windstress, and the river discharge found using the entire dataset at once is acceptable ( $r^2= 60.3\%$ ) for the near-field plumes, but it is almost insignificant ( $r^2= 14.5\%$ ) in the case of far-field plumes. In general, the linear fit hardly represented the data points in a plot of the plume area versus the river discharge. The linear relations found using the seasonal datasets suggested that a generalization (i.e. using the full-dataset) of the runoff-area-windstress relation implies an underestimation the plume area during the period January-March and an overestimation during the rest of the year.

In general, the river runoff was positively correlated with plume size. The effect of windstress was to enhance the effect of runoff in the near-field plumes, whereas in the far field, the effect of windstress was to oppose the effect of runoff.

In contrast to near-field plumes, the far-field plumes showed a monthly-mean variability that is adequately consistent with the windstress and runoff variability. However, some discrepancies were found in several months. It is thus believed that these discrepancies might be related to short-term variations of the wind direction, and the influence of residual currents and tides on the plume dynamics.

It is worth noting that, the windstress as treated in this study is a measure of the momentum transfer from the atmosphere to the oceans, and so, in one hand it promotes the mixing between fresh and saline waters and, on the other hand it contributes to the plume advection (according to the Ekman transport theory). Therefore, through these processes, the wind can contribute for the plume size growing, shrinking, or both depending on the wind direction and intensities. As a result, it is vital to conduct a similar study considering the variations in the wind direction.

### 6.4.2. Comparison with model results

According to the Chao's (1988) classification, the plumes observed on July 19<sup>th</sup> and 21<sup>st</sup> are of supercritical and subcritical type, respectively. This is slightly different from the model estimate, since the model has suggested that the plumes are of supercritical type for all river discharge and windstress conditions. The reason for this discrepancy might be the fact that, the model overestimates the plume's coastal flow, and as a result, the freshwater is continuously advected out of the model domain. Due to fact that the freshwater movement within the model is unbounded, the generation of broader coastal flows (i.e. transversally wider than the bulge length) cannot take place.

It is important to note from the observation results that, while the runoff measured at Tete takes 17 days to cause changes in the size of the near-field plumes, it takes a shorter time (7 days) to cause changes in the size of the far-field plumes. In its turn, the model estimates indicated a runoff time-lag of about 8 days for the far-field plumes, suggesting that for this type of plumes, the model and the observations adequately agree. In spite of this agreement, the fact that the freshwater alters the far field plumes earlier than the near field plumes constitute an inconsistency. It is thus believed that this inconsistency in the time-lag is somewhat related to mixing processes in the vicinity of the river mouth, though, no conclusive result was found from the analysis of the windstress.

It must be clear that the comparison between modeled and observed plume areas is a matter that is far beyond the scope of this study, since the model was designed for unreal plumes uniquely. On the other hand, the relationship between the plume area and river discharge is addressed. The linear relations established either using the model or the observations have presented a common feature: a positive slope, being equal to 1.73 s/m and 1.74 s/m for the model and observation estimates, respectively. The error committed when using the model to derive the slope was found to be insignificant (error=0.6%). Judging from the significance of a slope in a linear relation, it is suggested that the model proposed in this study is a powerful tool for understanding the dynamics of a river plume and its associated effects.

In addition, the model failed to reproduce the intercept of such relation, with a remarkable error of 280%. The primary reason for such a huge error is the fact that the model predicts a negative intercept, while the observations reveal a positive intercept of the relation. A negative intercept suggests the existence of threshold of river discharge below which, no plume can be observed. A positive intercept represent the smallest value of the plume area, i.e. area for a zero discharge. Besides, the fact that the coefficient of determination of the linear relation found using the observations is as slight as 41.3% is likely to have some influence on the error estimate.

## CHAPTER 7

### CONCLUSIONS AND RECOMMENDATIONS

#### 7.1. General

This thesis has covered a study of the dynamics of the Zambezi River plume, in particular the relationship between the river discharge and the area of the consequent plume. Two different methods were used: numerical modelling and satellite observation.

A simple-physics 2D vertically-integrated particle-tracking two-layer model with a random component was developed for the Zambezi influenced coastal waters. The model considers a finite number of discrete freshwater particles, released at intervals of 30 minutes and not allowed to interact with the saline water.

The satellite observation was based on the ocean colour, in particular the normalized water-leaving radiance at two wavelengths. Despite the high level of cloud contamination in a great number of available images, it was possible to use the high-resolution satellite imagery to identify and quantify the plumes in the vicinity of the Zambezi River. The MODIS images were processed in *Matlab*, and the statistical analysis performed in *Minitab* environment.

Both the model results and the satellite observations were favourable for increasing the insight into the effects of windstress and river discharge on the surface trapped plumes.

The conclusions that were drawn from this study are summarised in the following section. The final section gives recommendations for future study.

## 7.2. Conclusions

- The type of the plume generated by the Zambezi River is classified as “large scale plume” and therefore, the plume dispersion patterns are primarily defined by the Coriolis Effect. The direction and intensity of local winds are the second most predominant factor controlling the dispersion patterns.
- The relation between the Zambezi river discharge and the corresponding plume area is time-dependent. To some extent, both satellite observations and simulations have showed that the relation during January-March is linear with a slope of 1.73 s/m (model) and 1.74 s/m (observation). During this period, the effect of windstress on the plume size is negligible.
- The Zambezi plumes have a coefficient of persistence  $k = -0.9$ , meaning that the plume size only increases if the freshwater volume discharged per day is greater than 90% of the volume discharged during the preceding day. In other words, 90% of the freshwater volume discharged per day is diluted during the day.
- The area of the near-field plumes is less responsive to the influence of winds than the area of the far-field plumes is. In general, the windstress is inversely proportional to the plume size.
- The river discharge measured upstream at Tete takes about 7-8 days to influence the size of the far-field plumes.

### 7.3. Recommendations

This thesis has led to the following recommendations:

- The arguments presented in this study are centred on the approximation that the red/blue  $nL_w$  is a good proxy for salinity. Current studies on the relation between salinity and the ratio of reflectance, conducted in a number of locations, report accuracies of about 95-99%. Since the reflectance in some wavelengths is highly affected by the concentration of phytoplankton in the water, which in turn varies seasonally, it is recommended that the time-dependence in the salinity algorithm is examined and reported in future studies.
- Apart from the dynamics factors mentioned in this study (the river discharge, the Coriolis deflection, and the winds), several studies have reported the residual coastal currents as being the most predominant factor in explaining the plume dispersion patterns. It is thus important to determine the influence of the residual coastal current on the size variability of the Zambezi River plumes.
- Regarding the area-discharge relationship, it is recommended that field measurements be taken in order to (i) analyze the size of the plume under extreme discharge conditions; and (ii) validate the coefficients of the linear relation between salinity and remotely sensed reflectances.
- In a considerable number of images, the limit between the Zambezi river plumes and the Buzi River (further south) plumes were hard to identify, because the waters near the Buzi occasionally presented the highest values of the red/blue  $nL_w$ . It is then recommended that the contribution of the Buzi freshwater to the hydrodynamics in the Sofala bank be addressed in future study.
- In order to improve the simulations, it is recommended to take the vertical diffusion of properties into account, i.e. to introduce a third coordinate and therefore, compute the mixing processes taking place.

---

**REFERENCES**

- Allen, J.I., 1997. A modelling study of ecosystem dynamics and nutrient cycling in the Humber plume, UK. *Journal of Sea Research*, 38: 333-359.
- Binding, C.E. and Bowers, D.G., 2003. Measuring the salinity of the Clyde Sea from remotely sensed ocean colour. *Estuarine, Coastal and Shelf Science*, 57 605-611.
- Bourgeois, S., Kocher, T. and Schelander, P., 2003. Zambezi River basin. In: T. Bernauer, B. Wehrli and A. Wüest (Editors), *ETH Seminar: Science and Politics of International Freshwater Management 2003/2004*.
- Bowers, D.G., (*unpublished work*). Model of Zambezi plume dynamics (1997), Maputo.
- Bowers, D.G. and Brett, H.L., 2007. The relationship between CDOM and salinity in estuaries: An analytical and graphical solution. *Journal of Marine Systems*, (in press).
- Bowers, D.G., Harker, G.E.L., Smith, P.S.D. and Tett, P., 2000. Optical Properties of a Region of Freshwater Influence (The Clyde Sea). *Estuarine, Coastal and Shelf Science*, 50: 717-726.
- Brakel, W.H., 1984. Seasonal Dynamics of Suspended-Sediment Plumes from the Tana and Sabaki Rivers, Kenya: Analysis of Landsat Imagery. *Remote sensing of environment* 16: 165-173.
- Chao, S.Y., 1988. River-forced estuarine plume. *Journal of Physical Oceanography*, 18: 72-88.
- Cheng, R.T. and Casulli, V., 2004. Modeling a three-dimensional river plume over continental shelf using a 3D unstructured grid model. In: S.M. L (Editor), *Eighth International Conference on Estuarine and Coastal Modeling*, Monterey, California, pp. 1027-1043.
- de Kok, J.M., 1996. A two-layer model of the Rhine plume. *Journal of Marine Systems*, 8: 269-284.
- Del Castillo, C.E. and Miller, R.L., 2008. On the use of ocean color remote sensing to measure the transport of dissolved organic carbon by the Mississippi River Plume. *Remote Sensing of Environment*, 112 836-844.
- Dias, J.M., Lopes, J.E. and Dekeyser, I., 2001. Lagrangian Transport of Particles in Ria de Aveiro Lagoon, Portugal. *Phys. Chem. Earth*, 26(9): 721-721.
- DiMarco, S.F. et al., 2002. Volume transport and property distributions of the Mozambique Channel. *Deep-Sea Research II* 49: 1481-1511.
- Dimou, K.N. and Adams, E.E., 1993. A random-walk, particle tracking model for well-mixed estuaries and coastal waters. *Estuarine, coastal and shelf science*, 37: 99-110.
- Fong, D.A. and Geyer, W.R., 2002. The alongshore transport of freshwater in a surface-trapped river plume. *Journal of Physical Oceanography*, 32: 957-972.

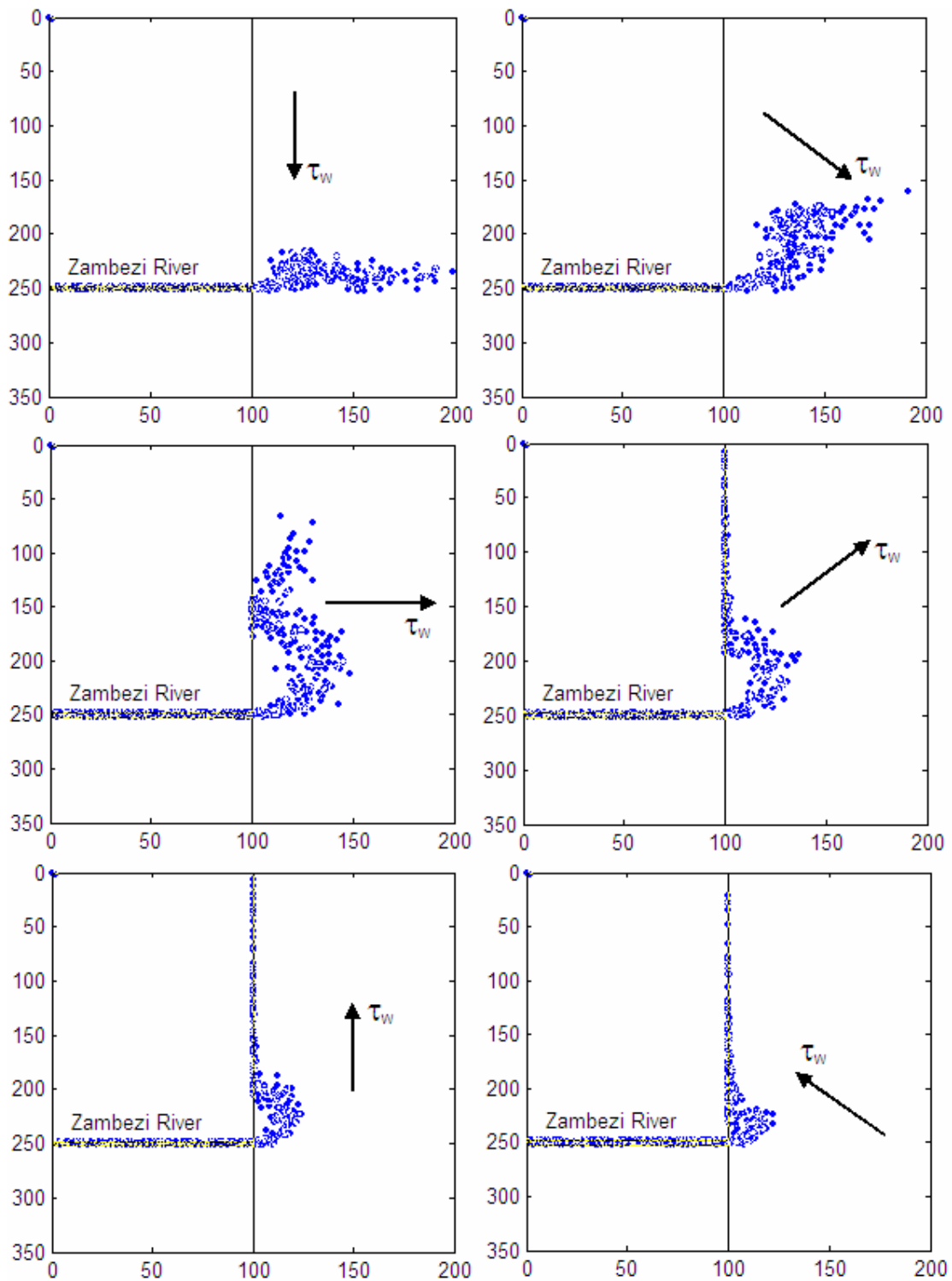
- Fong, D.A., Geyer, W.R. and Signell, R.P., 1997. The wind-forced response on a buoyant coastal current: Observations of the western Gulf of Maine plume. *Journal of Marine Systems*, 12: 69-81.
- Fong, D.A. and Stacey, M.T., 2003. Horizontal dispersion of a near bed coastal plume. *Journal of Fluid Mechanics*, 489: 239-267.
- Gammelsrød, T., 1992. Variation in Shrimp Abundance on the Sofala Bank, Mozambique, and its Relation to the Zambezi River Runoff. *Estuarine, Coastal and Shelf Science*, 35: 91-103.
- Garvine, R.W., 1995. A dynamical system for classifying buoyant coastal discharge. *Continental Shelf Research*, 15: 1585-1596.
- Garvine, R.W., 1999. Penetration of buoyant coastal discharge onto the continental shelf: A numerical model experiment. *Journal of Physical Oceanography*, 29: 1892-1909.
- Geyer, W.R., Hill, P., Milligan, T. and Traykovski, P., 2000. The structure of the Eel River plume during floods. *Continental Shelf Research*, 20: 2067-2093.
- Geyer, W.R. et al., 2004. The freshwater transport and dynamics of the western Maine coastal current. *Continental Shelf Research*, 24: 1339-1357.
- Gomez-Gesteira, M. et al., 1999. A two-dimensional particle tracking model for pollution dispersion in A Corufia and Vigo Rias (NW Spain) *Oceanologia Acta*, 22(2): 167-177.
- Hoguane, A.M., 1997. Shrimp abundance and river runoff in Sofala Bank - The rule of Zambezi. , Presented at "Workshop on Sustainable Use of the Cahora Bassa Dam", Songo, Mozambique (29 Sept. - 2 Oct,1997).
- Liu, W.-C., Chen, W.-B., Cheng, R.T. and Hsu, M.-H., 2008. Modelling the impact of wind stress and river discharge on Danshuei River plume. *Applied Mathematical Modelling*, 32: 1255-1280.
- Manikiam, B., Gowda, H.H., Manavalan, P., Jayaraman, V. and Chandrasekhar, M.G., 1993. Study of sediment dynamics using satellite remote sensing. *Adv. Space Research*, 13(5): (5)75-(5)78.
- Mann, K.H. and Lazier, J.R.N., 1991. Dynamics of marine ecosystems - Biological-physical interactions in the oceans. Blackwell Scientific Publications, Boston.
- Marinone, S.G., Ulloa, M.J., Parés-Sierra, A., Lavín, M.F. and Cudney-Bueno, R., 2008. Connectivity in the northern Gulf of California from particle tracking in a three-dimensional numerical model. *Journal of Marine Systems*, 71: 149-158.
- Marsaleix, P., Estournel, C., Kondrachoff, V. and Vehil, R., 1998. A numerical study of the formation of the Rhone River plume. *Journal of Marine Systems*, 14: 99-115.
- Mckee, D., Cunningham, A. and Dudek, D., 2007. Optical water type discrimination and tuning remote sensing band-ratio algorithms: application to retrieval of chlorophyll and  $K_d(490)$  in the Irish and Celtic Seas. *Estuarine, Coastal and Shelf Science*, 73: 827-834.
- Mélin, F., Zibordi, G. and Berthon, J.-F., 2007. Assessment of satellite ocean color products at a coastal site. *Remote Sensing of Environment*, 110: 192-215.

- Mestres, M., Sierra, J.P. and Sánchez-Arcilla, A., 2007. Factors influencing the spreading of a low-discharge river plume. *Continental Shelf Research*, 27: 2116-2134.
- Münchow, A. and Garvine, R.W., 1993. Buoyancy and wind forcing of a coastal current. *Journal of Marine Research*, 51: 293-322.
- Nezlin, N.P. and DiGiacomo, P.M., 2005. Satellite ocean color observations of stormwater runoff plumes along the San Pedro Shelf (Southern California) during 1997–2003. *Continental Shelf Research*, 25: 1692–1711.
- Nezlin, N.P., DiGiacomo, P.M., Stein, E.D. and Ackerman, D., 2005. Stormwater runoff plumes observed by SeaWiFS radiometer in the Southern California Bight. *Remote Sensing of Environment*, 98: 494 - 510.
- Nikiema, O., Devenon, J.-L. and Baklouti, M., 2007. Numerical modeling of the Amazon River plume. *Continental Shelf Research*, 27: 873-899.
- Odriozola, A.L. et al., 2007. On the absorption of light in the Orinoco River plume. *Continental Shelf Research*, 27: 1447-1464.
- Piñones, A. et al., 2005. Wind-induced diurnal variability in river plume motion. *Estuarine, Coastal and Shelf Science*, 65: 513-525.
- Sætre, R., 1985. Surface currents in the Mozambique Channel. *Deep-Sea Research*, 32. (12): 1457-1467.
- Sætre, R. and Silva, A.J.d., 1984. The circulation of the Mozambique Channel. *Deep-Sea Research*, 31(5): 485-508.
- Scodanibbio, L. and Mañez, G., 2005. The World Commission on Dams: A fundamental step towards integrated water resources management and poverty reduction? A pilot case in the lower Zambezi, Mozambique. *Physics and Chemistry*, 30: 976-983.
- Sentchev, A. and Korotenko, K., 2005. Dispersion processes and transport pattern in the ROFI system of the Eastern English Channel derived from a particle-tracking model. *Continental Shelf Research*, 25: 2294-2308.
- Siddorn, J., 1998. The use of colour algorithms in predicting the salinity of Zambezi river influenced coastal waters, University of Wales, Bangor, UK, 81 pp.
- Siddorn, J.R., Bowers, D.G. and Hogue, A.M., 2001. Detecting the Zambezi River plume using Observed Optical Properties. *Marine Pollution Bulletin*, 42(10): 942-950.
- Stabenau, E.R. and Zika, R.G., 2004. Correlation of the absorption coefficient with a reduction in mean mass for dissolved organic matter in southwest Florida river plumes. *Marine Chemistry*, 89: 55- 67.
- Vignudelli, S., Santinelli, C., Murru, E., Nannicini, L. and Seritti, A., 2004. Distributions of dissolved organic carbon (DOC) and chromophoric dissolved organic matter (CDOM) in coastal waters of the northern Tyrrhenian Sea (Italy). *Estuarine, Coastal and Shelf Science*, 60: 133-149.
- Warrick, J.A., DiGiacomo, P.M., Weisberg, S.B., Nezlin, N.P., Mengel, M., Jones, B.H., Ohlmann, J.C., Washburn, L., Terrill, E.J., Farnsworth, K.L., 2007. River plume patterns

and dynamics within the Southern California Bight. *Continental Shelf Research*, 27: 2427-2448.

Warrick, J.A., Mertes, L.A.K., Washburn, L. and Siegel, D.A., 2004. A conceptual model for river water and sediment dispersal in the Santa Barbara Channel, California. *Continental Shelf Research* 24: 2029-2043.

Warrick, J.A., Washburn, L., Brzezinski, M.A. and Siegel, D.A., 2005. Nutrient contributions to the Santa Barbara Channel, California, from the ephemeral Santa Clara River. *Estuarine, Coastal and Shelf Science*, 62: 559-574.

**APPENDICES****I. The effect of wind direction on the Zambezi plume****Figure 1:** Hypothetical distribution of freshwater particles under different wind

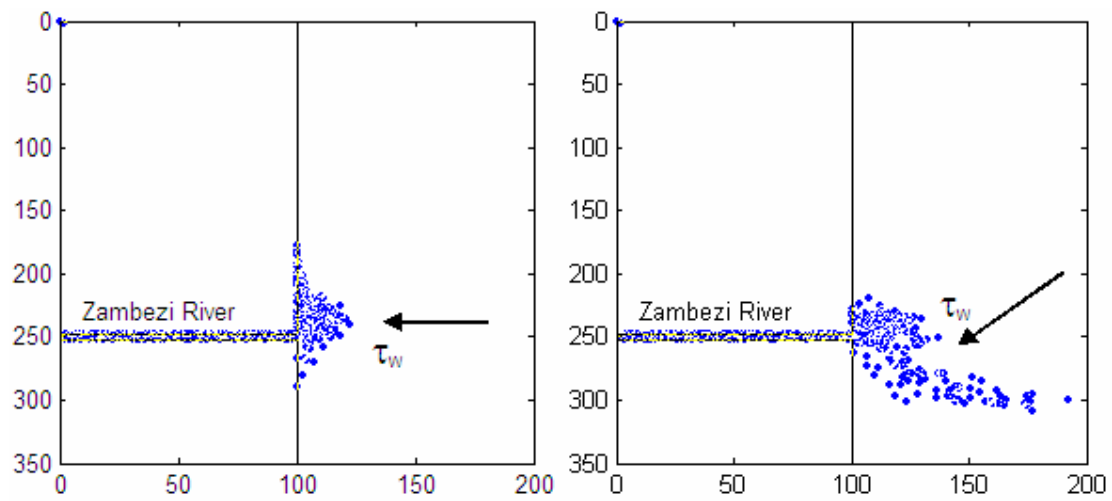


Figure 1 continued.

## II. Flags

**Table 1:** Contamination sources of the satellite derived radiances. The stars indicate the flags used in this study.

| Bit | Name       | Description                                    |
|-----|------------|--|
| 1   | Atmfail    | Atmospheric correction failure *               |
| 2   | Land       | Pixel is over land *                           |
| 3   | Badanc     | Reduced quality of ancillary data              |
| 4   | Higlint    | High sun glint *                               |
| 5   | Hilt       | Observed radiance very high or saturated       |
| 6   | Hisatzen   | High sensor view zenith angle *                |
| 7   | Coastz     | Pixel is in shallow water                      |
| 8   | Neglw      | Negative water-leaving radiance retrieved      |
| 9   | Straylight | Stray light contamination is likely            |
| 10  | Cldice     | Probable cloud or ice contamination *          |
| 11  | Coccolith  | Coccolithofores detected                       |
| 12  | Turbidw    | Turbid water detected                          |
| 13  | Hisolzen   | High solar zenith *                            |
| 14  | Hitau      | High aerosol optical thickness                 |
| 15  | Lowlw      | Very low water-leaving radiance (cloud shadow) |
| 16  | Chlfail    | Derived product algorithm failure              |
| 17  | Navwarn    | Navigation quality is reduced                  |
| 18  | Absaer     | possible absorbing aerosol (disabled)          |
| 19  | Tricho     | Possible <i>trichodesmium</i> contamination    |
| 20  | Maxaeriter | Aerosol iterations exceeded max                |
| 21  | Modglint   | Moderate sun glint contamination               |
| 22  | Chlwarn    | Derived product quality is reduced             |
| 23  | Atmwarn    | Atmospheric correction is suspect              |
| 24  | Darkpixel  | Rayleigh-subtraced radiances is negative       |
| 25  | Seaice     | Possible sea ice contamination                 |
| 26  | Navfail    | Bad navigation                                 |
| 27  | Filter     | Pixel rejected by user-defined filter          |
| 28  | Sstwarn    | SST quality is reduced                         |
| 29  | Sstfail    | SST quality is bad                             |
| 30  | Hipol      | High degree of polarization                    |
| 31  | Spare      | Spare  |
| 32  | Ocean      | not cloud or land                              |